This is to certify that the
dissertation entitled

Scanning tunneling microscopy of complex electronic
materials

presented by

Aleksandra T. Tomic

has been accepted towards fulfillment
of the requirements for the

Ph.D. degree in Physics and Astronomy

Stuart Tess
Major Professor's Signature

3/4/08
Date

DATE DUE	DATE DUE	DATE DUE

SCANNING TUNNELING MICROSCOPY OF COMPLEX ELECTRONIC MATERIALS

By

Aleksandra T. Tomic

A DISSERTATION

Submitted to
Michigan State University
in partial fulfillment of the requirements
for the Degree of

DOCTOR OF PHILOSOPHY

Department of Physics and Astronomy

2008

ABSTRACT

SCANNING TUNNELING MICROSCOPY OF COMPLEX ELECTRONIC MATERIALS

By

Aleksandra T. Tomic

I present results of experiments aimed at investigating two complex electronic systems, $CeTe_3$ and β-$K_2Bi_8Se_{13}$, utilizing scanning tunneling microscopy (STM) and scanning tunneling spectroscopy (STS) methods. In these systems, the electronic properties of interest are a charge density wave (CDW) state and thermoelectricity, respectively.

STM and STS measurements of $CeTe_3$ at room temperature and 77 K were performed, resulting in the first atomically resolved images of the material. Clear patterns showing the superposition of the atomic lattice and the charge density wave were resolved. The CDW wave length is incommensurate with the atomic lattice. The nature of this incommensurate state is a key question. It may be that the incommensurate CDW state is uniformly incommensurate, or that it is locally commensurate within domains and undergoes phase slips at the domain walls. The phase slips are called discommensurations. We have analyzed the Fourier transform of the STM images to test for signatures of discommensurations. Some Fourier peaks may be interpreted as evidence for discommensurations. However, a more compelling interpretation leads to the conclusion that the STM data is insufficient to discern discommensurations. In contrast, the atomic pair distribution function analysis gives evidence for discommensurations. The local density of states using the STS mode was measured at 77 K, and the CDW gap was observed at various places on the surface of the sample. The gap size measured directly above the Te atoms is ~360 meV. The CDW gap of YTe_3 was obtained from room temperature STS, and was estimated to be roughly ~320 meV.

$K_2Bi_8Se_{13}$ is a narrow band gap semiconductor and a promising thermoelectric material. The local electronic structure near the Fermi level of β-$K_2Bi_8Se_{13}$ was studied in STS mode. This crystal has a needle-like structure; in particular four chains of atoms form within the unit cell along the c direction. These are structural features of interest in this material, that significantly influence the electronic structure and narrow the band gap. STS measurements at 1.6 K temperature revealed a gap of approximately 0.4 eV, in good agreement with results of theoretical calculations. Further, the STS study revealed the presence of subgap states that, according to recent electronic band structure calculations exploring several K/Bi chain configurations, occur due to disorder along the chains. The disorder in β-$K_2Bi_8Se_{13}$ could play an important role for its thermoelectric properties, by changing the density of states near the band gap and potentially increasing the thermopower.

To my family

Acknowledgments

I would like to express my utmost gratefulness to my thesis adviser, Professor Stuart H. Tessmer, for all his help, guidance, patience, as well as for financial support during my graduate studies.

Unreserved gratitude and thanks to my thesis committee members, Professors S. D. Mahanti, Simon J. L. Billinge, Michael Thoennessen, and Carl Schmidt for their help during my studies and for their time and effort while being on the committee.

Significant contributions of Professor Mercouri G. Kanatzidis in various segments of the project presented here are acknowledged and greatly appreciated. Samples used in this study were provided by Kanatzidis group, and were synthesized by Christos Malliakas and Theodora Kyratsi. I thank them for their kind help.

Collaboration and discussions with HyunJeong Kim, Khang Hoang, and Zsolt Rak, are greatly appreciated, and I thank them for their kind help.

Many thanks to my dear friend and colleague Irma Kuljanishvili, and colleagues Morewell Gasseller, Cemil Kayis, and Josh Veazey for their companionship in the lab and their kind help.

I would like to thank my husband Emil Bozin for support and encouragement throughout the course of my graduate studies.

Finally, I thank my family for all the support, understanding and love, especially to my mother Vera Tomic for all her motherly help and support.

This work was supported by the National Science Foundation through Grant No. DMR-0305461, and by the Center for Fundamental Materials Research at Michigan State University.

Contents

List of Tables

List of Figures

Chapter 1

Introduction and Motivation

Solid state physics has been challenged by the discovery of new classes of complex materials in the past two decades. The degree of structural complexity and the delicate interplay between structural, electronic and magnetic effects yield fascinating physical properties such as high-temperature superconductivity in doped copper oxides [1], colossal magnetoresistance in manganites at high doping [2], and enhanced thermoelectric properties in novel thermoelectric materials [3]. Although these materials are important for potential technological applications, much of the physics behind corresponding phenomena is still not fully understood. It has recently been realized that features such as nanoscale inhomogeneities [4, 5, 6, 7, 8] and charge density waves [9, 10, 11, 12, 13] could play an important role in the physics of these important materials.

The degree of complexity of these materials and associated phenomena requires an approach that involves multiple experimental techniques probing different aspects of these phenomena, such as scanning tunneling microscopy (STM), which probes local electronic structure, and diffraction based techniques, that provide structural information. In addition, comparison of the experimental results with theoretical calculations is crucial for better understanding of the physics of these materials.

The STM technique is a powerful tool for studies of the nanoscale electronic structure of novel complex materials. Although STM is still a relatively new technique [14, 15], it has revolutionized surface science, and has been successfully employed in resolving local structure and spectroscopy of many materials of interest. In STM, atomic-scale spatial resolution can be achieved allowing for detailed studies of crystal surface topography, as well as local probing of the electronic structure. It is based on the quantum mechanical effect of electron tunneling through a vacuum barrier between two conductive electrodes.

In this work, I present results of experiments utilizing scanning tunneling microscopy in two specific complex systems. In these systems, electronic properties are of interest in the context of charge density wave states and thermoelectric properties, respectively.

The charge density wave (CDW) state, which is one of the fundamental broken-symmetry ground-states of metals [16], is most common in systems with reduced dimensionality. The CDW represents a spontaneous periodic spatial modulation of charge density across a material, with an associated deformation of the crystal lattice. The CDW state in materials is characterized by a gapped Fermi surface. A CDW is said to be incommensurate when the ratio of the CDW wavelength to the atomic lattice is an irrational number. Incommensurate CDWs exhibit nonlinear transport properties that can be utilized for potential applications [17]. It is very important to characterize the precise nature of the CDW in systems in which they occur. We employed STM in the surface topographic imaging mode and point spectroscopy mode to study the charge density wave state in $CeTe_3$ at various temperatures. Although $CeTe_3$ is a simple, layered system with a one-dimensional incommensurate CDW, the exact nature of the incommensurability in this material is not fully understood, as the CDW could either be uniformly incommensurate, or could be locally commensurate with discommensurations. In this work, STM is used to observe the CDW, to determine the CDW gap size, and to address the nature of the incommensurate

CDW.

Thermoelectric materials are those materials that can be utilized for conversion of temperature gradient to electric potential difference and vice versa. Good thermoelectric materials require large electrical conductivity, large thermopower, and small thermal conductivity [18]. Optimization of these parameters is often difficult [19]. Narrow band-gap semiconductors show great promise for future thermoelectric materials, as their properties can be tuned by doping. Electrical conductivity and thermopower are determined by the details of the electronic properties including the size and structure of the semiconductor band gap and scattering of charge carriers by defects and impurities, while thermal conductivity is affected by scattering of phonons. Therefore, resolving the electronic structure of thermoelectric materials is key to understanding their properties. We used scanning tunneling spectroscopy to study the the electronic structure of β-$K_2Bi_8Se_{13}$, which is a promising thermoelectric material. In particular, the band gap of β-$K_2Bi_8Se_{13}$ obtained using optical measurements in the infrared regime at room temperature [20] showed marked disagreement with the results of theoretical calculations [21]. In order to resolve this issue, I measured the band gap of this important material using STM. The observed electronic structure is also considered in relation to the nature of structural disorder on specific atomic sites that is believed to play an important role for its thermoelectric properties.

1.1 Thesis outline

The thesis is organized as follows. Chapter 2 represents a description of the STM experimental technique, including explanations of different modes used to carry out experiments and various experimental details. Chapter 3 reviews relevant physics related to the CDW phenomenon, with an overview of CDW types and of typical experimental methods sensitive to the CDW state. Chapter 4 brings the detailed results of the STM characterization of the CDW state in $CeTe_3$ at room temperature and 77 K. The basics of the physics of thermoelectric materials is given in Chapter 5, as well as the STM results of the electronic structure of β-$K_2Bi_8Se_{13}$ at 1.6 K temperature. Concluding remarks and possible directions for further work are given in Chapter 6.

Chapter 2

Scanning Tunneling Microscopy

2.1 Basic principles of STM

2.1.1 Introduction

Scanning tunneling microscopy (STM) is a technique developed in the early 1980s, after the first tunneling signal through a controllable vacuum gap had been achieved by Binnig, Rohrer and collaborators [14]. This was followed by the demonstration of successful surface microscopy using vacuum tunneling, producing the first topographic pictures of surfaces on an atomic scale. Examples of resolved monoatomic steps and surface reconstructions were shown by the same group for surfaces of Si, $CaIrSn_4$ and Au [15]. STM is now routinely used for surface imaging as well as for local probing of the electronic structure of materials.

The operation of the STM is based on the quantum mechanical effect of electron tunneling through a vacuum barrier between two conductive electrodes. The tunneling current starts to flow when a sharp tip of the STM probe is brought in proximity of a conducting surface, at a distance of approximately 0.5 nm. A polarity of a voltage applied between the tip and the sample surface determines the direction of the tunneling current. The magnitude of the tunneling current decays exponentially as the tip-sample separation increases. The STM technique can only be applied to study

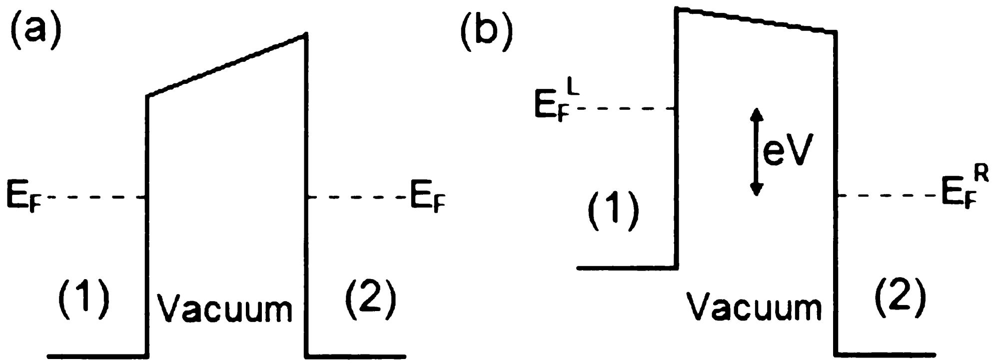

Figure 2.1: Conducting electrodes (1) and (2) in close proximity: when unbiased, the Fermi levels equilibrate and take the same value E_F (a). When bias voltage V is applied the Fermi levels split by eV and become E_F^L and E_F^R (b).

conducting or semiconducting samples, as for the insulating samples the electrons have no available energy states to tunnel into or out of due to the insulating band gap.

2.1.2 Tunneling in STM

Consider two conducting electrodes (1) and (2) at a temperature of absolute zero. When the separation between the two electrodes is small enough to allow tunneling, the electrodes come into an electrical equilibrium, such that there is a unique Fermi level for both of them, as shown in Figure 2.1(a). When a bias voltage V is applied across the two electrodes, the Fermi levels split by energy eV, where e is the electron charge, as shown in Figure 2.1(b), and directed quantum tunneling can occur. States within an energy interval eV separating the two Fermi levels contribute to the tunneling, with electrons occupying filled states within eV below the higher Fermi level of one electrode tunneling into the empty states within eV above the lower Fermi level in the other electrode [22]. At finite temperatures transient tunneling can occur even when no voltage is applied as some of the electrons in the electrodes will be thermally excited above the Fermi level. On average, this effect cancels as tunneling occurs in both directions between the electrodes.

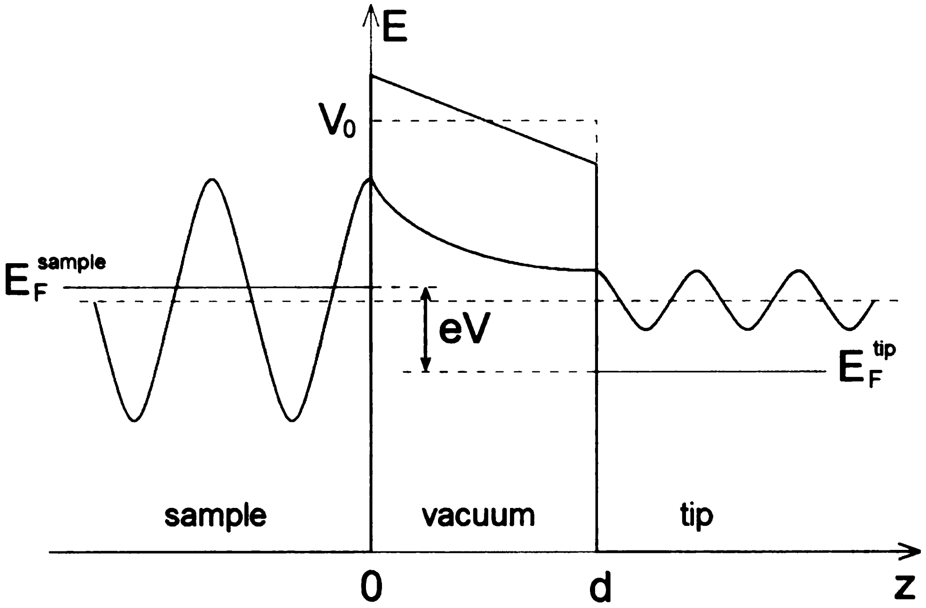

Figure 2.2: The vacuum barrier of width d between the sample and the tip, shown with the electronic wavefunction. Bias voltage V is applied, and the Fermi levels E_F of the sample and the tip are separated by eV. The electronic wavefunctions are periodic in the sample and the tip, and decay exponentially in the vacuum region.

Here I provide a simple illustration of the quantum tunneling effect which is a basis of the STM operation. Consider a rectangular barrier, such as that shown in Figure 2.2, which is a reasonable approximation if the bias voltage is small compared to the work functions of the tip and the sample. The work function is defined as $\phi = V_0 - E_F$, where V_0 is the potential in the barrier. For simplicity I will assume a one dimensional tunneling barrier, with the dimension denoted z. For such a barrier the electron motion is governed by the time independent Schrödinger equation

$$-\frac{\hbar^2}{2m}\frac{d^2\psi}{dz^2} + V_0\psi = E\psi. \qquad (2.1)$$

If the electrons are incident on the barrier from the left, then there are three branches for the solution to the Schrödinger equation as follows:

$$\psi(z) = \begin{cases} A\exp(\frac{ipz}{\hbar}) + B\exp(\frac{-ipz}{\hbar}), & z < 0 \\ C\exp(-kz) + D\exp(kz), & 0 \le z \le d \\ \tau\exp(\frac{ip(z-d)}{\hbar}), & z > d \end{cases} \tag{2.2}$$

where $p = \sqrt{2mE}$ and $\hbar k = \sqrt{2m(V_0 - E)}$. At the boundaries of the three regions these functions and their first derivatives must be continuous, which sets constraints on the choice of constants. Furthermore, the value of constant D is exponentially suppressed, to avoid the unphysical solution of the wave function diverging in the case of a thick barrier.

In the STM system the two electrodes are the tip and the surface of the sample, where the separation between them is less than 1 nm. As implied from Eq. 2.2, the electron wavefunction is sinusoidal in the sample and the tip, but *decays exponentially* inside the barrier as $\psi(z) = C\exp(-kz)$. The wavefunction of the transmitted electrons is $\psi(z) = \tau\exp(\frac{ip(z-d)}{\hbar})$, where τ is the transmission coefficient. If the barrier is sufficiently thick, the slope of the exponentially decaying function $\psi(z)$ is close to zero at the vacuum-tip interface. Due to continuity conditions of ψ and $\frac{d\psi}{dz}$, it follows that the value of the wavefunction at $z = d$ is $\psi(d) = C\exp(-kd) = |\tau|$. As the tunneling current I is proportional to the transmission probability $|\tau|^2$ [23], it follows that

$$I \propto \exp(-2kd). \tag{2.3}$$

2.1.3 STM resolution

As the tunneling current depends exponentially on separation between the tip and the sample, one readily sees that the STM is extremely sensitive to small variations in the tip-sample spacing. This is called z-sensitivity. When the separation between the tip and the sample changes by Δd, then the tunneling current changes by a factor of $\exp(-2k\Delta d)$, as seen from Equation 2.3. For example, for the typical value of work function of ϕ=4 eV, the value of $k = \frac{\sqrt{2m(V_0-E)}}{\hbar}$ for states at Fermi level is 1.03 Å^{-1}. An increase of Δd=1 Å in the separation between the tip and the sample would cause the tunneling current to drop by factor of $\exp(-2k\Delta d) = 0.127$, i.e., an *order of magnitude.* Atomic resolution of STM is a direct consequence of the z-sensitivity: if one atom at the apex of the tip is 1 Å closer to the sample than the other atoms, most of the tunneling current will flow through that apex atom. As it is shown by Stoll *et al.*, most of the tunneling current is typically confined to a small area with a radius of approximately 3 Å on the sample surface, which is sufficient to detect the corrugation of individual atoms [24].

2.2 Frequently used STM methods

The STM technique was initially developed to investigate the surface topography properties of materials on the atomic scale. However, fairly soon after it was established, STM was employed for probing of the local electronic structure as well. Essentially, there are three parameters that can be varied: the applied bias voltage between the tip and the sample, the tunneling current, and the tip position with respect to the sample. The ability to vary these parameters enables the STM probe to be useful for characterization of different properties. There are two common modes of STM operation. One mode is the *constant current mode*, also referred to as the *surface topographic imaging.* The second mode of operation is *scanning tunneling spectroscopy* (STS) in *point spectroscopy mode.*

2.2.1 Surface topographic imaging mode

In the surface topographic imaging mode, the tip is scanned over the surface of the sample while the tunneling current is maintained constant. A fixed bias voltage is applied and the desired tunneling current is set. As the tip is scanned across the surface of the sample, variations in the topography of the sample and the underlying electronic structure affect the tunneling current. In order to keep the preselected value of the tunneling current constant, a feedback circuit is used to adjust the position of the tip above the sample surface. Feedback voltage, corresponding to the vertical position of the tip is recorded, reflecting the surface topography. Details are described in Section 2.3.

2.2.2 Scanning tunneling spectroscopy

In the point spectroscopy mode, the position of the STM tip is kept fixed with respect to the sample surface, over a single point of the sample. The bias voltage V is ramped, typically from -300 mV to +300 mV, and the tunneling current I is measured as a function of the ramped voltage V. Differentiation of $I(V)$ with respect to V provides a direct measure of the sample's *density of states* at a temperature of absolute zero. At finite temperatures, the measurements are *smeared* by 3.5 k_BT, where k_B is the Boltzmann constant, and T is the measurement temperature. To minimize the smear out of the data, the STM spectroscopy is typically operated cryogenically. At liquid ^{4}He temperature, 4.2 K, we can resolve details of the electronic structure of the sample on a sub-meV energy scale. Since materials that are subject of this study are expected to have band gaps of the order of hundreds of meV, the energy resolution of the measurements allows for the energy band structure to be determined with exceptional quality.

To illustrate the principle behind the electronic structure measurements in the spectroscopic mode of STM, we will follow a simple set of equations. In order to obtain an expression relating tunneling current to the electronic structure, we assume that all tunneling transitions occur at constant energy where states within an energy interval eV separating the two Fermi levels contribute to the tunneling [23]. We can calculate the total tunneling current by adding up all contributions from each energy level. For temperatures $T > 0$, the number of occupied states in the sample electrode at the given energy E is $N_s(E)f(E)$, where $N_s(E)$ is the density of states of the sample electrode and $f(E)$ is the Fermi function. The number of empty states in the tip electrode, at the same energy E, is given by $N_t(E - eV)(1 - f(E - eV))$, where $N_t(E - eV)$ is the density of states of the tip electrode. As electrons from the occupied states can tunnel only into empty states, the tunneling current from the sample to the tip can be written as

$$I_{s \rightarrow\, t} \propto \int_{-\infty}^{\infty} |\tau|^2 N_s(E) f(E) N_t(E - eV)[1 - f(E - eV)]dE, \tag{2.4}$$

where

$$f(E) = \frac{1}{exp(\frac{E}{k_B T}) + 1} \tag{2.5}$$

represents the Fermi function for a state with energy E. For temperatures $T > 0$, thermal excitations bring electrons into states above the Fermi energy. Thermally excited electrons in the sample electrode leave the empty states. Thermally excited electrons in the tip electrode can tunnel into these emptied states, creating the tunneling current from the tip to the sample

$$I_{t \rightarrow\, s} \propto \int_{-\infty}^{\infty} |\tau|^2 N_t(E - eV) f(E - eV) N_s(E)[1 - f(E)]dE. \tag{2.6}$$

The quantity $|\tau|^2$ is the transmission probability for tunneling from the initial to a final state. We can approximate that the transmission probability is independent of energy E if only energies close to the Fermi energy are considered. Therefore $|\tau|^2$ can be immersed into the constant of proportionality. The total tunneling current is the difference between the current from the sample to the tip and the current from the tip to the sample:

$$I \propto \int_{-\infty}^{\infty} N_s(E) N_t(E - eV)[f(E) - f(E - eV)]dE, \tag{2.7}$$

To simplify the equation we will assume that the STM tips, typically made of noble metals such as *Au* or *Pt*, have *constant* density of states near the Fermi level, i.e., N_t is independent of E. Differentiation of I with respect to V then gives

$$\frac{dI(V)}{dV} \propto \int_{-\infty}^{\infty} N_s(E)[-\frac{\partial f(E - eV)}{\partial(eV)}]dE. \tag{2.8}$$

When $k_B T \rightarrow 0$, then

$$\frac{\partial f(E - eV)}{\partial(eV)} \rightarrow \delta(E - eV) \tag{2.9}$$

leading to

$$\frac{dI(V)}{dV} \propto N_s(eV) \tag{2.10}$$

when $T \rightarrow 0$. Thus at low temperatures, differentiation of I with respect to V gives a direct measure of the sample's density of states.

2.3 STM design

An important aspect of the exponential decay of the tunneling current with increased sample-tip separation is that it sets spatial limitations to the tunneling range of the microscope. If the tip is too far away from the sample, no tunneling can occur, as the tunneling probability will be negligible. Therefore, bringing the tip into tunneling range and scanning it over the sample surface requires extremely precise control. Since the invention of scanning tunneling microscopy, the issue of tip and sample control was part of the design, and significant improvements of stability and performance of the STM have been achieved over the years.

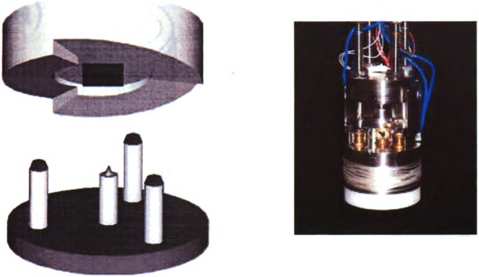

Figure 2.3: Scheme and photograph of the scanning tunneling microscope, based on a design by K. Besocke [25]. The sample holder is resting on three piezoelectric tubes. The central piezotube is holding the tip. The sample is located above the tip (dark square).

The control of the sample-tip separation is typically achieved by using a series of electrically controlled piezo-tubes. These materials utilize the piezoelectric effect, which represents the ability of crystals and certain ceramic compounds to generate a voltage in response to applied mechanical stress. Conversely, piezoelectric crystals, when subjected to an externally applied voltage, can change their shape by a small amount. The piezoelectric effect has numerous applications, such as high voltage and power generation, sensors, actuators, reduction of vibrations, production and detection of sound, electronic frequency generation, micro-balances, and ultra fine focusing of optical or electronic assemblies, such as STM.

The design of the scanning tunneling microscope used in this study (Figure 2.3) is based on the design developed by K. Besocke [25], which provides excellent stability utilizing a compact assembly. Moreover, the design achieves very small thermal drift by using a thermally compensated geometry. Figure 2.3 shows a schematic of the design and a photograph of the microscope. The position of the tip with respect to

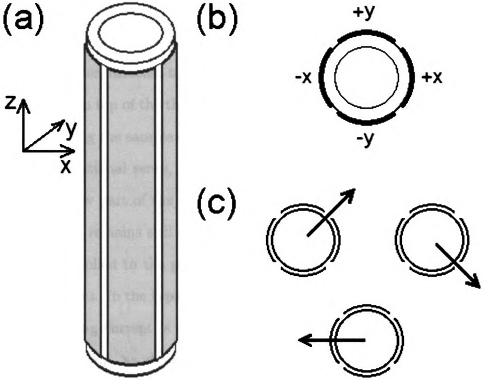

Figure 2.4: (a) Schematic representation of a typical STM piezotube with four quadrants. (b) The top view: the quadrants denoted with +X, +Y, -X, and -Y are used for the electromechanical control. (c) Schematic of the three carrier piezotubes indicating motion in rotational sense.

the sample is controlled by small piezoelectric tubes. The sample holder is resting on three carrier piezoelectric tubes in a triangular configuration. The carrier piezotubes have smooth stainless steel balls on the top, used for contact with the sample holder. These piezotubes bring the sample into tunneling range of the tip. The tip is attached to the central piezotube (also called scanning tube), which is used to scan the tip over the surface. Each of the piezotubes is metallized to form four quadrants, as shown in Figure 2.4(a) and Figure 2.4(b), that can each change dimensions independently. The tube is lengthened or shortened by applying a positive or negative voltage on all the quadrants simultaneously, providing the motion in the z direction. For motion in the lateral direction, one quadrant is lengthened while the opposite one is shortened, causing the tube to bend in the x or y direction. For our microscope at room temperature the sensitivity of the piezoelectric ceramics is 200 Å/V, providing the maximum scan range of about 5 μm in the x and y directions.

The sample holder, directed toward the tip, contains three sloped ramps (see Figure 2.3) that slide on top of the three piezotubes, as controlled by the electromechanical system, and bring the sample closer to or away from the tip. This is accomplished by motion in a rotational sense, as seen in Figure 2.4(c), using a sawtooth-like signal. During the slow part of the signal, the sample holder rotates together with the piezotubes, while it remains still during the fast part of the signal.

The voltages applied to the piezotube quadrants are controlled by commercially purchased electronics. In the typical mode of STM operation, *constant current mode*, the desired tunneling current is maintained by controlling tip-to-sample separation by using feedback loop, as shown in Figure 2.5. An amplifier with 10^9 V/A gain is used to convert the low tunneling current between the tip and the sample to a voltage signal. This is compared to the preset voltage corresponding to the desired value of the tunneling current. The difference between these two voltages is used to create a feedback voltage as follows. The difference signal, or error signal, is sent into a feedback circuit. The feedback voltage is generated as a combination of two components: the first is called gain, and is directly proportional to the error signal; the second one, called time constant, is proportional to the integral of the error signal. The feedback voltage is sent to the piezoelement controlling the z position of the tip, resulting in an adjustment of the tip position to correspond to the preset tunneling current. The tunneling current is typically set to a range of 0.1-1 nA.

A high value of the gain results in a faster response of the feedback loop, while a low gain would result in a relatively slow response. However, if the value of the gain is set too high and the integrator too low, the system may over correct, which will cause the current to oscillate around the set value. This phenomenon is known as feedback oscillation. It can be particularly troublesome if too much noise is present

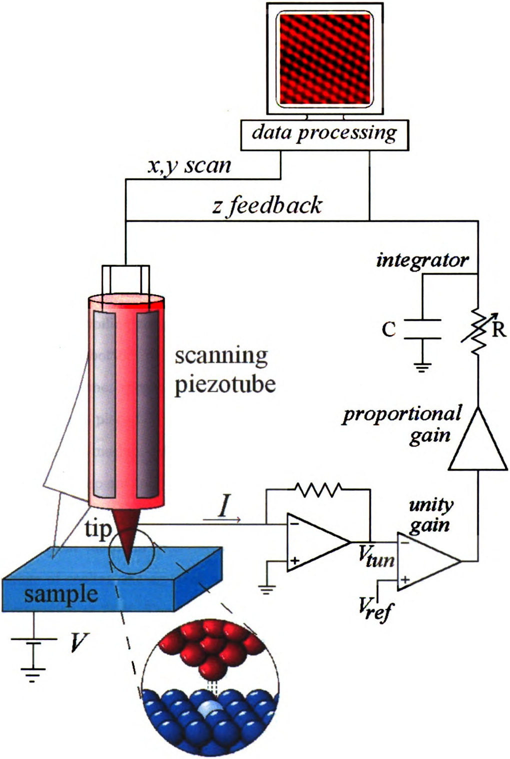

Figure 2.5: Schematic representation of the STM feedback circuit.

in the signal. This undesirable mode is corrected by resetting the values of the gain and time constant. The typical gain varies between the values of 0 and 2. Typical value of the feedback time constant varies between 1 and 20 ms.

2.4 Cryogenic system

The STM experiments can be performed at room temperature as well as at selected low temperatures using a cryogenic system. In this project we employed a ^{3}He cryogenic system, Figure 2.6, which operates at liquid nitrogen temperature (77 K), liquid ^{4}He temperature (4.2 K), at the temperature of liquid ^{3}He around 1.2 K, which could be further lowered to the base temperature of 0.270 K by lowering the vapor pressure to decrease the boiling temperature of ^{3}He. The scanning tunneling microscope is mounted to the bottom of a long stainless steel probe which is used to lower the microscope into the cryogenic system. To prepare for a data run at room temperature, the probe is placed on the top of the cryostat and the sample area is evacuated by using a turbo-mechanical pump to achieve high vacuum. Cooling the cryostat to liquid helium temperature of 4.2 K is done in stages. In the first stage, the cryostat is cooled down to 77 K with liquid nitrogen. The liquid nitrogen is then completely evacuated from the main reservoir, and the cryostat is filled with liquid ^{4}He. The first stage of cooling the cryostat with liquid nitrogen could be maintained for the STM operation at 77 K. The probe is lowered into the sample space of the cryostat, which is kept in vacuum. After lowering into the sample space, the probe requires approximately 10-15 hours for thermal equilibration.

The base temperature of the cryogenic system operation of 0.270 K is achieved by reducing the vapor pressure of the liquid ^{3}He which is initially at temperature of 1.2 K. Before proceeding to the base temperature, the cryogenic system has to be cooled to liquid ^{4}He temperature. Gaseous ^{3}He is then allowed to enter the sample space from the ^{3}He storage dump, but it is trapped inside the sorb, a cold massive

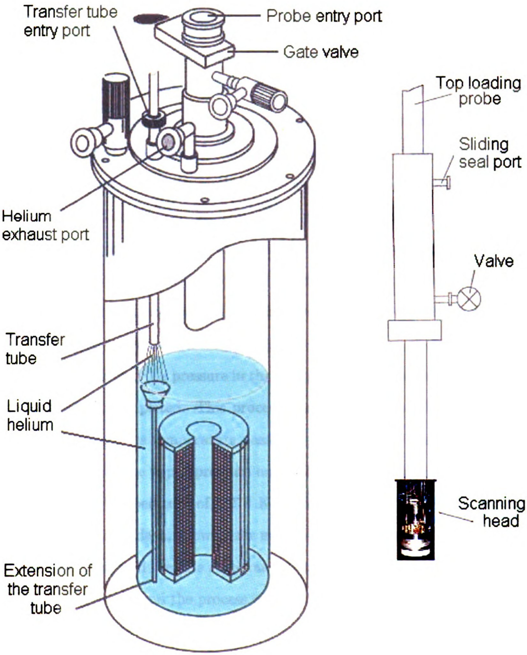

Figure 2.6: Schematic representation of our STM cryogenic setup.

charcoal pump in the sample space. By warming up the sorb slightly, a few mbar of ^{3}He gas is introduced into the sample space as an heat exchange gas. The scanning tunneling microscope, mounted to the probe, is then lowered to the bottom of the sample space. Lowering the microscope needs to be done slowly in order to protect the piezoelements from thermal stress. Outside of the sample space, attached to its walls, is a donut shaped chamber called 1 K pot. The 1 K pot is used for condensation of ^{3}He and for keeping the measuring system cold. The pot is not in the direct contact with the main liquid ^{4}He reservoir, the connection is achieved only through a thin tube for ^{4}He delivery, so the pot could be run at varying temperatures. With a flow of about 2 l/min of liquid ^{4}He through the pot and by lowering the pressure in the pot to about 20 mbar, the 1 K pot temperature lowers to a minimum of 1.2 K.

When the sorb is warmed to about 30 K temperature, gaseous ^{3}He is released from the sorb. This ^{3}He hits the cold copper piece of the probe (which is in a contact with the 1 K pot), condenses on it and drips into the ^{3}He pot at the bottom of the sample space. When the ^{3}He pressure in the sample space reaches its minimum value, the condensation is completed. This procedure requires about 1 hour. The sorb is then cooled down. As its temperature passes 15 K it starts to pump the remaining ^{3}He gas, and reduces the vapor pressure and boiling temperature of the liquid ^{3}He. This way the base temperature of 0.270 K is achieved. The base temperature can be maintained for three days, allowing for measurements at cryogenic temperature to take place, after which all the ^{3}He evaporates. At that moment all ^{3}He molecules are trapped inside the sorb, and the process can be repeated.

2.5 Mechanical stability of STM

It has been shown in Sections 2.1.2 and 2.1.3 that the tunneling current changes by almost an order of magnitude for a change in tip-sample separation as small as 1 Å. Considering the sensitivity of the STM, good mechanical isolation of the microscope from all external vibrations is a critical issue. The surrounding environment of the STM probe, such as the building, the people and the machinery, are all common sources of noise, with amplitude of mechanical vibrations of the order of a few thousand angstroms. Keeping the tunneling current stable requires tip-sample mechanical vibrations to be limited to amplitudes less than 0.1 Å. Such mechanical stability is achieved by use of compact STM design and an efficient dual-stage isolation system. The compact STM design, discussed in Section 2.3, gives high normal-mode vibration frequencies $\sim$ 1 kHz, which are not easily excited by room vibrations ($\sim$ 10-20 Hz).

Mechanical decoupling of the STM probe from the ambient vibrations is achieved with the dual-stage external vibration isolation system. The first stage of the isolation consists of four donut shaped rubber air springs, and the second stage consists of four specialized hydraulic shock-absorbing legs, frequently used to support tables with delicate optical measurement setups. These two stages may be modeled as a dual stage oscillating system of simple springs which results in an increase of the damping factor, important for achieving necessary stability of STM. Acoustic vibrations are also observed to have the effect on stability of the tunneling current. In addition to the system assigned to dampen mechanical vibrations from the experimental floor, our laboratory STM room is cushioned with sound absorption padding on the walls, to cut down on acoustic reverberation. The cushion contains patterned sheets of sound-insulating material arranged in checkerboard pattern, to most efficiently dampen all the sounds propagating through the experimental room.

Other dominating sources of noise are STM tip instabilities and various defects and impurities on the sample surface. The STM tips used in this study were commercially purchased from Materials Analytical Services, Inc.

The experiments were performed with fresh chemically etched tips, as well as with in-house mechanically cut tips. In both cases, the tips are made of alloyed platinum and iridium in a 80/20 ratio. These tips do not oxidize, which is important for stability of the experiment when tunneling is performed in the air. Typical length of the tip is 1.0(1) cm, with the wire diameter of 0.25 mm. The top part of the STM tip is tapered. It is about 200 μm long with the radius of curvature of the very end of 50 nm. Although the tips are prepared in the same way, using the same method, not all of the tips perform equally well. There is no simple method of evaluating and predicting the performance of the tip other than to test its performance once it is mounted on the STM. The tip stability is one of the first parameters to ensure successful experimental performance. In the cases when the tip is unstable, due to a tunneling through a loose atom on a tip, or because some particles are attached to it, the STM images are usually streaky. Unstable tip conditions could sometimes be improved by a process of 'shaking' the tip, which is a fast scanning with a maximum possible scan range, for about 10 minutes. Another commonly used process is field emission where a sudden increase in bias voltage causes the electric field to eject loose particles on the tip. Of course, if these measures are unsuccessful, the tip has to be exchanged with a new one.

Cleanness of the surface of the sample is another important issue influencing the stability, as the tip can interact with impurities and become unstable. Samples to be studied are therefore carefully cleaved with scotch tape or a razor blade, such that layers are tightly packed without loose flakes, allowing for a fresh surface to be probed. If weakly attached layers are present on the sample surface, the tunneling current is unstable due to electric field forces acting on them. The samples used in this study were prepared in the air, and then transferred into a loading chamber and evacuated with a turbo-mechanical pump. Although the samples were exposed to air for about 5 minutes, the experimental tests that were carried out indicated that the surfaces were sufficiently inert such that the contamination is negligible.

2.6 System testing and calibration

After the new STM tip is mounted on the probe and before experiments are conducted, routine tests have to be performed. These tests are required to ensure good performance of the tip as there is no other special way to evaluate it. The typical sample to use in the tests is graphite. Obtaining atomic resolution images of graphite demonstrate that the tip is acceptable. Graphite crystals consist of the layers of carbon atoms. In each layer, carbon atoms are covalently bonded into hexagons, while different layers are connected together by weak van der Waals forces. Carbon atoms on the graphite surface appear in the STM images as a triangular lattice which contains every other atom, not as honeycomb rings as it would be expected. Figure 2.7(a) is the STM image of graphite surface where triangles of three carbon atoms are visible, while the other three atoms are missing. This asymmetry was explained by Tomanek *et al.* as a purely electronic effect due to the interlayer interactions [26]. It was explained as having two nonequivalent carbon atom types in each layer. Carbon atoms of one type have neighbors directly beneath them in the underlying atomic layer. Carbon atoms of the second type do not have neighbors directly beneath them. Band structure calculations predict that atoms visible in the STM image are ones that do not have the subsurface atom beneath them.

The sensitivity of piezo material in the scanning tube depends on the geometry and polarization. We use graphite samples and a structured platinum sample to properly calibrate our piezotubes. Graphite is used for getting lateral sensitivity: the STM image of graphite with good atomic resolution is used to obtain correct value of the scan range, knowing that graphite plane lattice constant is 2.46 Å. For the particular STM image, the applied voltage to the scanning piezotube for motion in the lateral direction is known. The lateral sensitivity of the piezotube is then determined as a measure of lateral displacement per one volt. The platinum sample is useful for z-calibration. This sample is patterned into a mesh of squared pits. A value used for

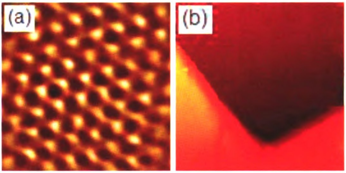

Figure 2.7: (This figure is presented in color.) (a) Carbon atoms in the STM image of graphite surface at the scan range of 24.4 Å x 25.8 Å , obtained at the tunneling current of 0.5 nA and the bias voltage of 100 mV. The image is cleared with Fourier filtering. (b) The STM image of platinum sample at the scan range of 5.8 μm x 5.7 μm, obtained at the tunneling current of 80 pA and the bias voltage of 180 mV.

z- calibration is the actual depth of the platinum pits of 180 nm. As the squared pits are 5 μm in size, with the same size of separation between them, there is an excellent chance of finding an edge, as it can be seen in Figure 2.7(b). Using the same method as for the lateral calibration, the z sensitivity of the piezotubes can be obtained.

Chapter 3

Charge density waves

3.1 Introduction

The charge density wave (CDW) state is one of the competing ground states in anisotropic, low-dimensional materials. Among the phenomena that can occur in such materials are superconductivity, ferromagnetism, antiferromagnetism, and spin density wave states. The physics of charge density wave formation involves pronounced nesting vectors in the Fermi surfaces of these materials [22, 27], accompanied with the gapping of parts of the Fermi surfaces. The conduction electron density in nearly free-electron-like three-dimensional metals can be considered as highly uniform, while the equilibrium positions of the atoms in the underlying lattice form a perfectly periodic arrangement. Spatial variations of the electron density are strongly suppressed in these systems, as they require large Coulomb energy penalty. On the other hand, in systems with reduced dimensions static modulations of the electronic density are possible. In such materials, when the temperature decreases below a certain critical temperature, the crystal lattice spontaneously develops a periodic deformation due to electron-lattice coupling. In a self consistent manner, this results in a modulation in electron density with the same periodicity, which is accompanied by a rearrangement of the electronic bands such that the total energy of the system is lowered. Such modulation of the electron density is called a charge density wave [16].

The CDW phenomenon is usually observed in crystals of reduced dimensions, such as quasi-two-dimensional [28] and quasi-one-dimensional [16] materials. Well-known examples include inorganic layered materials like $NbSe_3$, $TaSe_3$, and $K_{0.3}MoO_3$, and quasi-one-dimensional organic conductors like tetramethyl-tetraselenafulvalene (TMTSF) or tetrathiafulvalene-tetracyanoquinodimethane (TTF-TCNQ). Periodic arrangements of charges have also been observed in various oxide systems, such as charge stripes in nickelates [29, 30], superconducting cuprates [12] and colossal magnetoresistive manganites [31], and checkerboard charge arrangements in cuprates [32, 33]. In the late 1990's the stripe phase observed in cuprate high temperature superconductors attracted considerable attention as long-range ordered charge stripes were found to correlate with the suppression of superconductivity [12]. Moreover, dynamically fluctuating stripe phases have been considered to be of central importance for an understanding of the physics of high-temperature superconductors [12, 34].

Compared with other conducting materials studied in bulk form, CDW conductors show an extremely rich variety of properties, like nonlinear and anisotropic electrical properties, unusual elastic properties, and gigantic dielectric constants. These properties make them interesting for potential applications such as CDW memory devices, switches, rectifiers, mixers, and optical detectors [35]. The organic CDW materials are of particular importance for studies of electrons in solids because their properties can be tuned at the synthesis stage [36].

3.2 Basics of the physics of CDWs

More than 50 years ago, R. E. Peierls introduced the theory of CDWs [37]. Peierls showed that the one-dimensional electron gas coupled to the phonon system becomes unstable at low temperature and undergoes a phase transition to an insulating state. The basic concept of this phenomenon resurfaced when the first anisotropic, low-dimensional materials became available. This was at the time when various organic materials were synthesized [38], starting with TTF-TCNQ [39], in which a set of long molecules donated electrons to another set leaving one-dimensional conductors with partially filled bands, presumably good candidates for superconductivity [40]. Surprisingly, with cooling, these materials became insulators rather than superconductors. That was the first experimental observation of this phenomenon, called the Peierls transition.

While all materials are three-dimensional by definition, in certain classes of materials, electrons are limited to moving easily along one direction in the structure, and are much less mobile perpendicular to it. In such a case the electron conductivity might be from 10 to 1000 times greater in the preferred direction [36]. Such materials are said to have quasi-one-dimensional character. Prerequisite for CDW formation is existence of such reduction of dimensionality, hence reduced dimensionality represents a common feature of all CDW materials [35].

3.2.1 The Peierls transition

The charge density wave represents a cooperative state in which both the crystal lattice and the electron gas exhibit a distortion to lower the total energy of the system. The periodic distortion of the lattice creates a supercell which reduces the kinetic energy of the highest energy occupied electrons of the conduction band. This energy gain, however, becomes relevant as the temperature is lowered below some critical temperature, T_{CDW}, where the effect of thermal excitations is reduced. If the total energy gain is sufficiently large to surpass the cost of distorting the lattice and the Coulomb energy, the charge density wave will form.

To illustrate the underlying physics behind the CDW formation, I will consider a one-dimensional metal at temperature $T = 0$. If electron-phonon interaction is not present, the ground state corresponds to the one shown in Figure 3.1(a). The

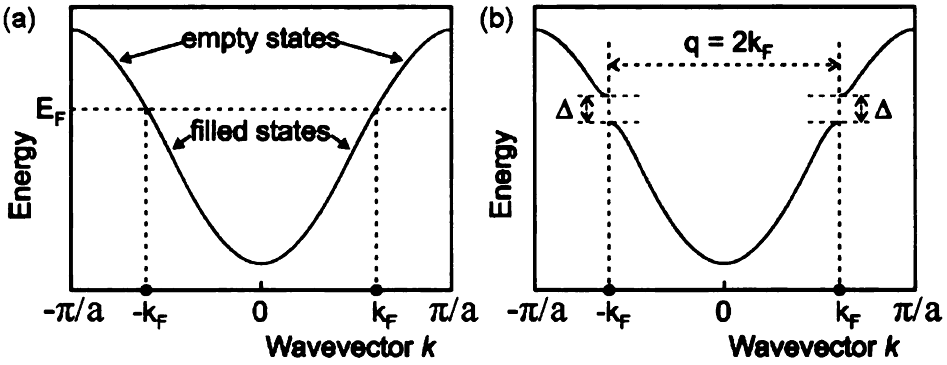

Figure 3.1: The conduction band of a one-one-dimensional crystal [42]. One-electron states with energy $E(\mathbf{k}) < E(\mathbf{k}_F)$ are filled, while states with $E(\mathbf{k}) > E(\mathbf{k}_F)$ are empty. (a) Periodic crystal with $\pm\pi/\mathbf{a}$ describing the boundary of the first Brillouin zone. (b) 1D crystal with a PLD with period $\mathbf{q} = 2\mathbf{k}_F$, showing an energy gap, Δ, in the dispersion at $\mathbf{k} = \pm\mathbf{k}_F$.

one-electron states of the conduction band are occupied up to the Fermi level E_F, while states above the Fermi level are empty. In the presence of electron-phonon interaction, the metal becomes unstable. Peierls showed that it was energetically favorable to introduce a periodic deformation of the lattice, with the period λ related to the Fermi wavevector $\mathbf{k}_F$ by $\lambda = \pi/\mathbf{k}_F$, corresponding to the wavevector $\mathbf{q}$ which is twice the Fermi wavevector, $\mathbf{q} = 2\mathbf{k}_F$ [37]. The periodic lattice deformation (PLD) is responsible for opening up a gap at the Fermi level, as shown in Figure 3.1(b). The energies of the occupied states below the Fermi energy E_F are lowered, while the empty states are raised in energy. The gain in electron energy is proportional to $u^2 ln(u)$ for small lattice distortions u, while the cost of strain energy is proportional to u^2 [41], thus explaining the stability of the deformed state.

As shown by Peierls [37], the CDW state is the preferred ground state in quasi-one-dimensional and quasi-two-dimensional metals at low temperature. This comes about as the cost in elastic energy to modulate the atomic lattice is smaller than the gain in conduction electron energy. At sufficiently high temperature the metallic state is stable, as the electronic energy gain competes with the thermal excitation of electrons across the gap. The second order phase transition that occurs between the metallic and CDW state at T_{CDW} is known as Peierls transition.

3.2.2 Fermi surface nesting

The Peierls instability is induced by strong electron-phonon interaction, which can develop due to the characteristic topology of the Fermi surface. In quasi-two dimensional or quasi-one-dimensional free-electron-like metals the Fermi surface is cylindrical or planar, and large areas of the Fermi surface can be separated by the same wavevector. The CDW state becomes most favorable when there are large number of states connected by the same $2\mathbf{k}_F$ vector. Such a vector of constant momentum transfer connecting parallel segments of Fermi surface is called a nesting vector [27]; similarly, the overlap of parts of the Fermi surface as a result of a translation of parts of the surface by a nesting vector is called Fermi surface nesting. The more the Fermi surface is nested, the more stable the CDW state is. To better understand this concept, consider a system of electrons in a single one-dimensional chain of atoms at $T = 0$. The Fermi surface for such a system consists of two points $\mathbf{k} = -\mathbf{k}_F$ and $\mathbf{k} = +\mathbf{k}_F$, and involves two states each due to spin. These are the states that would lower their energy when the CDW gap opens. If we have a two-dimensional system of n non-interacting parallel chains in a plane, this system can be considered quasi-one-dimensional and its Fermi surface comprises of two sets of colinear points along two parallel lines perpendicular to the direction of chains, $2\mathbf{k}_F$ apart. In such a case we have $4n$ states subject to lowering their energy by the gap opening, for the same expense in the elastic energy, thus lowering the total energy of the system. Similarly, for a three-dimensional, periodic distribution of non-interacting chains, the Fermi surface is made of two flat parallel planes perpendicular to (0, 0, $\pm k_F$), where the z-direction is the direction of the chains. In this case every point of the plane $(0, 0, -k_F)$ of the Fermi surface is connected with a point of the plane $(0, 0, k_F)$ by the vector $\mathbf{q} = (0, 0, q_z)$ with $q_z = 2k_F$, which is called perfect nesting. In such a case

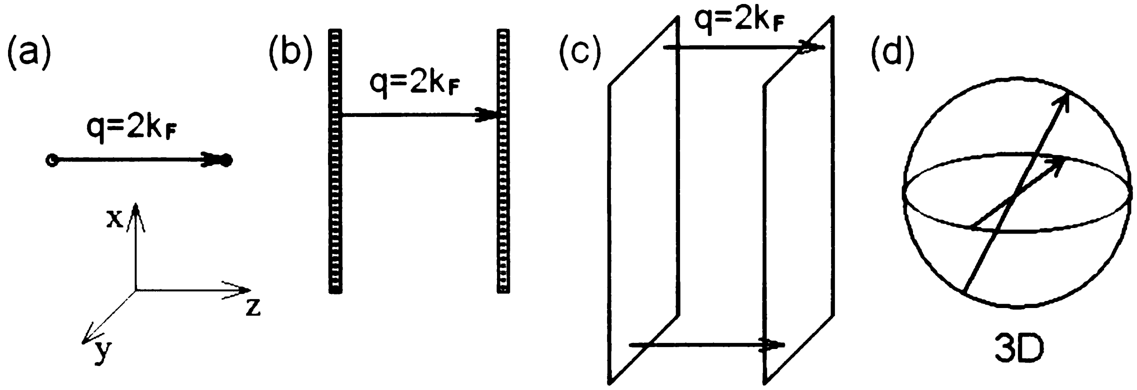

Figure 3.2: Fermi surface nesting in a free electron model. (a) In the case of a single 1D chain, the Fermi surface consists of two points. (b) In the 2D case of non-interacting parallel chains, the Fermi surface consists of two sets of colinear points along two parallel lines perpendicular to the direction of chains. (c) In 3D periodic distribution of non-interacting parallel chains, the Fermi surface consists of two planes perpendicular to the direction of the chains. (d) In 3D isotropic crystals, nesting is fulfilled for a single point on the spherical Fermi surface.

periodic lattice deformation with modulation wavevector **q** will lower the energy of all one-electron states below the Fermi surface. Then the CDW state, characterized by **q**, will have lower energy than the normal state. All three cases are illustrated in Figure 3.2 (a)-(c). On the other hand, in three-dimensional crystals, as shown in Figure 3.2(d), the nesting condition for each prospective vector **q** can be fulfilled only for a single point on the Fermi surface, and the gain in electronic energy for the few states near this point is *insufficient* to overcome the elastic energy cost.

In real systems containing one-dimensional metallic chains, there are always weak interactions between them, and the electron bands have a small dispersion in the directions perpendicular to the chains. The characteristic one-dimensional dispersion still remains parallel to the direction of chains. Any given vector **q** will then be a good nesting vector for only part of the Fermi surface. Only the nested fraction of the Fermi surface will become gapped, while the remaining part will keep the compound metallic [42].

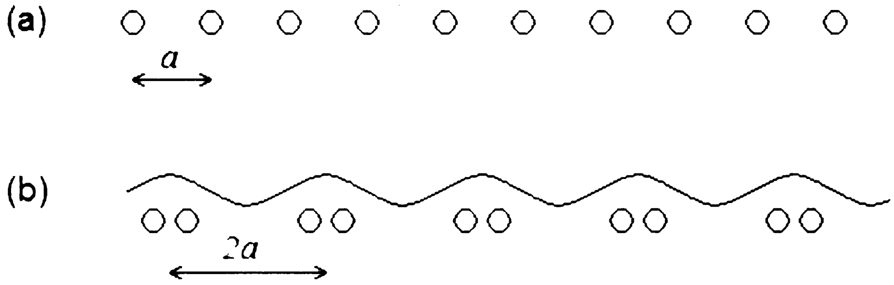

Figure 3.3: (a) For an undistorted one-dimensional metal with a half-filled band, the lattice is a periodic array of atoms with lattice constant a. (b) One-dimensional metal with a half-filled band, with introduced periodic lattice deformation and associated CDW with period $2a$.

3.3 CDW types

The character of a CDW depends on how its wavelength λ relates to the original lattice periodicity a, hence CDW is often characterized by the ratio λ/a. The CDW wavelength $\lambda = 2\pi/\mathbf{q}_{CDW} = 2\pi/2\mathbf{k}_F = \pi/\mathbf{k}_F$ depends on the number of electrons in the conduction band: if there are more electrons, the value of $\mathbf{k}_F$ increases and the CDW wavelength becomes smaller, and vice versa. For a crystal with a half-filled band, the CDW state corresponds to a periodic structure with a period that is twice as large as the periodicity of the crystal lattice, as seen in Figure 3.3. In general, however, the number of electrons in the conduction band is not related to the lattice periodicity, so the CDW wavelength could be any fraction of the lattice constant a.

When the ratio of the CDW wavelength λ and lattice constant a is an irrational number, the CDW state is said to be incommensurate. Then the CDW floats around and it is not affected by the lattice until pinned down by a defect; a defect acts like a pot-hole in which the CDW state gets stuck. On the other hand, when the ratio of the CDW wavelength λ and lattice constant a is a rational number, the CDW is commensurate with the lattice periodicity, and then it is hard to get it moving, as it is more likely to be pinned to the lattice. This is the reason why incommensurate CDWs show a variety of interesting physical properties.

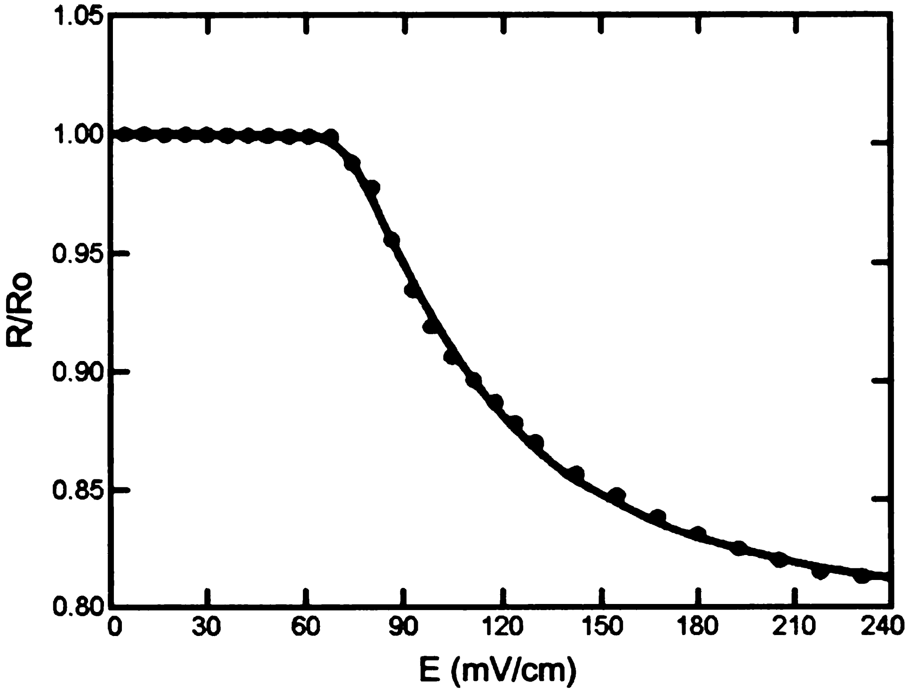

Figure 3.4: The normalized resistance $R/R_o = (1/R_o)dV/dI$, versus applied external electric field, E, in $NbSe_3$ [17]. V represents voltage, I is current, and R_o is the value of R at $V = 0$. For the low values of E the system obeys Ohm's law, $R/R_o = 1$. Above certain threshold field ($E_o = 117mV/cm$ in case of $NbSe_3$), the incommensurate CDW starts sliding, thus opening a second conduction channel, resulting in a decreased resistance $R/R_o < 1$.

The single-particle energy diagram is suggestive of CDW conductors being semiconductors: they have a band of filled states which is separated by an energy gap from a band of empty states. However, like superconductors, CDW conductors have a collective charge transport mode. When an external electric field is applied, the CDW can slide relative to the lattice. The lattice atoms oscillate back and forth, producing a traveling potential, and the conduction electrons move with this potential, producing a current. However, the CDW conductors are not superconductors, since various mechanisms damp the collective motion at nonzero temperature, leading to finite resistance. This is one of the most interesting properties of the incommensurate CDW: the nonlinear conductivity, as has been found in several CDW compounds [16]. For example, in $NbSe_3$ in the CDW state, non-linear electrical conductivity has been observed by Fleming [17]. When an external electric field is applied, for low values of the electric field, $NbSe_3$ obeys Ohm's law, as seen in Figure 3.4. Typically the sliding will not begin until a depinning threshold field is exceeded where the wave can escape from a potential well caused by a defect. Once the treshold is reached, a new conduction channel occurs due to the sliding of the CDW that results in enhancement of the conductivity. Hence the resistance drops below that given by Ohm's law. This property can be utilized for potential applications, such as extremely sensitive detectors of electromagnetic radiation if the applied field is tuned to drive the CDW close to the depinned state, where small changes in electric field cause abrupt changes in material's conductivity.

3.4 Methods of detection of CDWs in materials

The charge density wave state in materials can be observed and studied using various experimental methods that are sensitive either to the charge distribution, or associated lattice deformation, or some other physical property that is affected by the presence of the CDW. Here I provide a brief overview of some selected techniques and means by which these are used to detect the CDW state in materials.

Angle resolved photoemission spectroscopy (ARPES) is a surface probe and is a commonly used method for studying the electronic structure of complex systems [43]. It represents the technique of choice in order to assess with high resolution the energy and momentum phase space of the electrons. It is based on the photoelectric effect, and involves measurements of the kinetic energy and angular distribution of the electrons photoemitted from a sample illuminated with high-energy photons. The ARPES technique allows for deduction of information on energy band dispersion and Fermi surface of materials. It has been successfully used to study and characterize the transition to a CDW state in materials, such as that in quasi-two-dimensional KMo_6O_{17} [44], where partial CDW gap opening, as well as nesting of the Fermi surface were observed. This study revealed that in this material below T_{CDW} the carriers are removed from the Fermi surface, and transferred to higher binding energy states (those that are below the gap) [44]. ARPES can be used to estimate the nesting vector $q_{CDW} = 2k_F$.

Scanning tunneling microscopy (STM) is a surface probe that provides information about local density of electronic states at the Fermi level [14, 45]. STM allows the mapping of regions of high and low electron density and hence the observation of the CDW on the surface of the material directly [46]. In the spectroscopic mode, the technique can measure the size of the CDW gap as it opens when the material undergoes the transition from its normal to the CDW state. STM has been widely used to characterize the CDW state of variety of materials, such as $K_{0.9}Mo_6O_{17}$, where spectroscopic measurements revealed a strong decrease of the density of electronic states near the Fermi energy, indicating suppression of a fraction of the material's Fermi surface at temperatures below T_{CDW} [47].

The CDW state can be detected through transport measurements, where transport properties exhibit anomalous behavior. For example, in one of the most thoroughly studied CDW materials, $NbSe_3$, two distinct CDWs occur, at two transition temperatures. Figure 3.5 shows dc resistivity of $NbSe_3$, as obtained by Ong and Monceau [48], where two anomalous bumps are observed indicating formation of two independent CDWs in this system at 144 K and 59 K. Similarly, in KMo_6O_{17} resistivity measurements show a metal-metal transition at around T_{CDW}, seen as a bump in the resistivity curve, which reflects Peierls transition to a CDW state. This is due to a change of mobility of the charge carriers and to a decrease in the density of states at Fermi level, as the CDW gap opens up [44].

Diffraction based methods, utilizing x-rays [49], neutrons [50], or electrons [51] as a probe, provide information about the positions of the atoms, and are not particularly sensitive to the details of the charge distribution. However, these methods provide

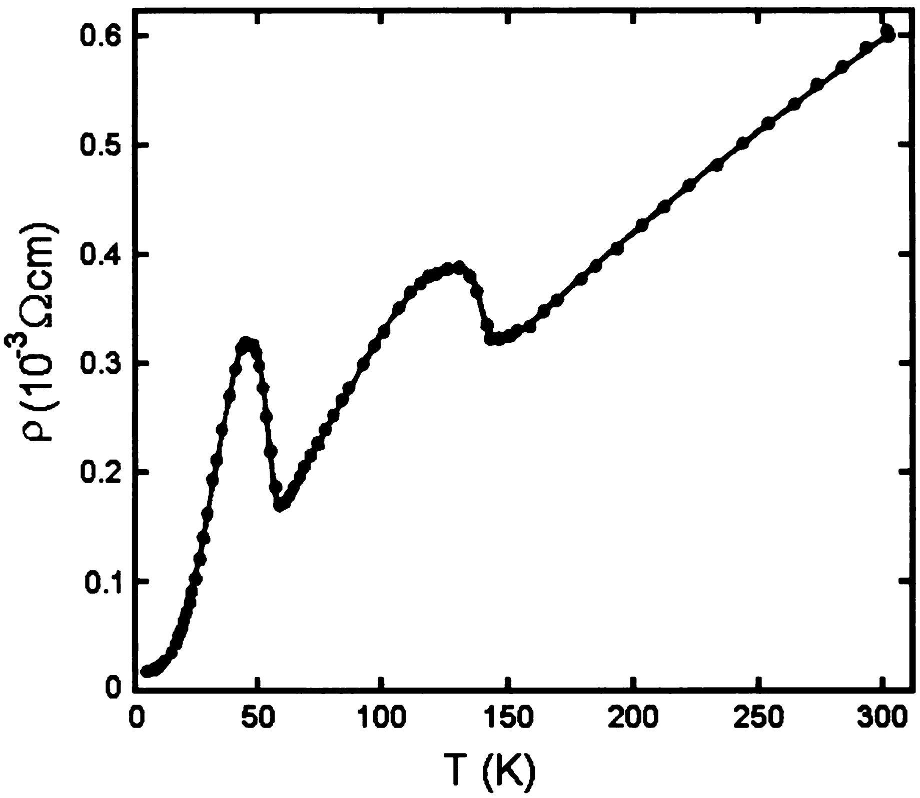

Figure 3.5: Anomalous transport properties of $NbSe_3$, as observed by Ong and Monceau [48]. Large increases of the dc resistivity appear at 144 K and 59 K, indicating the formation of two independent CDWs in this system.

valuable information related to the underlying periodic lattice deformation associated with the CDW. The periodicity $\mathbf{q}$ of the periodic lattice deformation is responsible for the occurrence of additional Bragg reflections, known as superlattice reflections, in the diffraction patterns at satellite positions $\pm\mathbf{q}$ around each Bragg reflection of the underlying basic structure [42]. For example, single crystal electron and x-ray diffraction studies on KMo_6O_{17} [52] demonstrated that periodic lattice distortions occur at low temperature and the diffraction patterns exhibit superlattice reflections below T_{CDW}.

The CDW state can also be studied using various spectroscopic methods, such as nuclear magnetic resonance (NMR) and Raman spectroscopy. Detailed account of these techniques is beyond the scope of this review. In a simplified view, the NMR method utilizes a strong magnetic field to align the magnetic nuclei in the structure under study, splitting the energy levels of the magnetic nuclei. An energy-variable electromagnetic field is then applied to the sample. For characteristic values of this field, that match the energy splitting caused by the magnetic field, resonance occurs. The result of the experiment is an NMR signal as a function of frequency [53]. It provides detailed information on the topology, dynamics and three-dimensional structure of magnetic species, spin density (NMR) and charge density (NQR) distribution in materials. In $NbSe_3$, the nature of CDW occuring at 144 K was studied using NMR spectroscopy [54]. This study revealed the nature of different Nb sites in this material in the normal state. Below T_{CDW} the NMR spectra gave line shapes that are broadened due to presence of a CDW, indicating that the CDW is incommensurate [54]. Raman spectroscopy provides information about vibrational, rotational, and other low-frequency phonon modes in solids [55]. It utilizes inelastic (or Raman) scattering of monochromatic laser light, typically in the visible, near infrared, or near ultraviolet range. The laser light interacts with phonons in the sample, which causes shifts in the energy (increase or decrease) of the laser photons. The shift in energy provides information about the phonon modes present in the system. Upon transition from normal to a CDW state in materials, changes occur in the spectrum indicating presence of the CDW state. For instance, in 1T-TaS_2 a CDW state is achieved at temperatures below 200 K. Hirata and Ohuchi studied Raman spectra from this material as a function of temperature between 48 K and 297 K using unpolarized laser light [56]. The study demonstrated that high-frequency modes in the spectra exhibit significant changes towards lower wavenumbers (and therefore lower energies) when T_{CDW} is approached on cooling.

3.5 Examples of CDW materials

Characterizing in detail the nature of the charge density wave state [57] as one of the possible broken symmetry and competing low-temperature ground states [58, 59] of low dimensional electronic systems is extremely important for understanding the physics of these materials [60]. It may also provide important insights into the nature of other competing states, such as high temperature superconductivity [28, 59, 61, 62]. Intensive research has been carried out on various layered systems, including $(TaSe_4)_2I$ [63, 64, 65, 66, 67], $NbSe_3$ [17, 68, 69, 70, 71], 1T-TaS_2 [72, 73, 74, 75, 76, 77], and 1T-$TaSe_2$ [78, 79, 80, 81] among many others. These systems, due to their low dimensionality, exhibit rich CDW behavior caused by the intrinsic electronic instability. For example, 2H-$NbSe_2$ exhibits an incommensurate CDW state below 33.5 K and remains in that state down to at least 5 K [78]. In 1T-$TaSe_2$ a commensurate CDW was observed, and is stable for a wide range of temperatures [82]. In 2H-$TaSe_2$ below 122 K an incommensurate CDW state was observed, and the CDW locks to a commensurate state at 90 K temperature [78]. Various CDW phases characterize 1T-TaS_2 over a wide temperature range [73, 83]. Above 543 K this material is in the normal phase [83]. It exhibits an incommensurate CDW for $353\ K < T < 543$ K [84, 85]. The nature of the CDW phase between $200\ K < T < 353$ K had been contraversial for quite some time, and the suspected characters were nearly commensurate (NC) [86, 87] and domain-like discommensurate (DC) structures [73, 88]. In the NC state the CDW is characterized by uniform amplitude and phase, while the corresponding lattice distortion is rotated with respect to the atomic lattice by 12°. On the other hand, in the DC model hexagonal domain-like structure is proposed such that the CDW is commensurate within domains that are ≈ 67 Å in size, separated by domain walls in which the CDW amplitude decreases and the CDW phase changes. The STM study of Wu and co-workers demonstrated that the DC model is the right one for describing the CDW state of 1T-TaS_2 at room temperature [73]. Below 200 K, 1T-TaS_2 is in a commensurate CDW state [75].

Chapter 4

Study of the charge density wave in $CeTe_3$

4.1 Introduction

Recently, the family of layered $RETe_3$ materials, where RE is a rare-earth element (RE = La, Ce, Pr, Nd, Sm, Gd, Tb, Dy, Ho, Er, Tm), has been recognized to belong to a class of two-dimensional CDW materials [89, 90, 91]. This class of materials exhibits two-dimensional square-net motifs composed of Te atoms in the structure. Such square-net arrangements have been considered theoretically (e.g. by Tremel and Hoffmann who performed electronic band structure calculations for such systems) [92] and were found to be unstable and prone to CDW formation. On the experimental side, results of transport measurements indicate that coupling between layers in $RETe_3$ is rather weak [93, 94]. Studies on different RE compounds revealed that for the electronic structure the rare earth is of minor importance [95]. This, in turn, suggests that the tellurium planes play a key role in determining the electronic properties of $RETe_3$. In this system, a CDW forms in tellurium layers that contain a square net of Te-atoms. However, the exact nature of the CDW in the $RETe_3$ family has not been resolved to date, and there is still an ongoing debate regarding

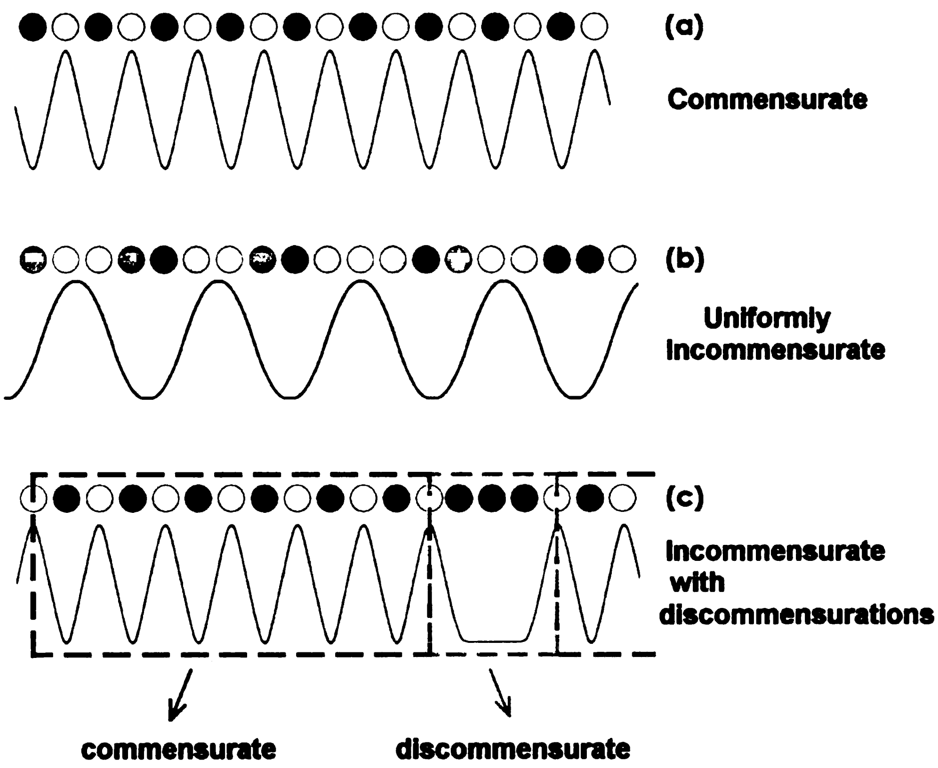

Figure 4.1: Schematic illustration of charge density waves along one-dimensional chains of atoms (circles and dots). The shading of each atom indicates its apparent magnitude with respect to an STM measurement, with white corresponding to a relatively high signal and black indicating a relatively low signal. Depending on the ratio of the CDW wavelength λ and atomic lattice a, the CDW can be (a) commensurate with λ/a rational, or (b) incommensurate with λ/a irrational. Part (c) shows the discommensurate case, for which an incommensurate CDW is locally commensurate - or locked in with the atomic lattice - with discommensurations (domain walls) preserving the average CDW wavelength.

whether the incommensurate CDW in RETe$_3$ is uniformly incommensurate or discommensurated as discussed below [96, 97]. Resolving this issue is of importance for better understanding of the physical properties, such as determining the strength of electron-lattice interaction.

In general, an incommensurate CDW state can take two forms depending on the nature of the CDW-lattice interaction. It could be uniformly incommensurate for which the CDW and the lattice modulations are simply superimposed. Alternatively, it is possible to achieve a state which is considerably more subtle, where the lattice and the CDW become locally commensurate within domains and undergo phase slips at the domain walls. The phase slips are called discommensurations and their role is to preserve the average incommensurate periodicities, as shown schematically in Figure 4.1. Discommensurations have been found in a variety of complex systems such as ferroelectrics [98], semiconducting monolayer surfaces [99], graphite compounds [100] and CDW dichalcogenide compounds [101].

One of the goals of this study is to look for evidence of discommensurations in the systems of interest. In this work we used STM and STS methods to characterize the CDW state of $CeTe_3$ and closely related YTe_3 at 300 K and 77 K temperature, and to determine the value of the CDW energy gap. To the best of our knowledge, these measurements yielded the first atomically-resolved STM data on these materials.

4.2 CDW and structure of $CeTe_3$

4.2.1 Ideal crystallographic structure of $CeTe_3$

Crystallographic structure of $CeTe_3$, shown in Figure 4.2, is of $NdTe_3$ [102, 103] type, weakly orthorhombic and described within the space group *Cmcm*. It is a layered structure that consists of two building blocks: double layers of $[Te]^-$ square-nets, and puckered ionic $[Ce_2^{3+}Te_2^{2-}]^{2+}$ double layers that are placed between the nets. Three-dimensional structure is composed of slabs of these structural motifs. The atoms within slabs are covalently bonded, while bonds between the slabs are weak van der Waals, allowing the crystals to cleave easily between the Te layers where the CDW forms, making them suitable for STM measurements. It should be noted that this structural view is an idealized representation, and is strictly speaking incorrect, as I further discuss.

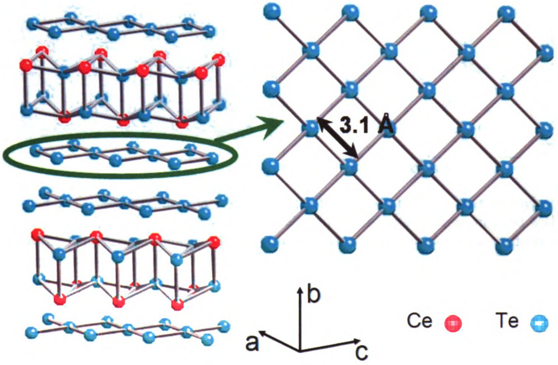

Figure 4.2: (This figure is presented in color.) The average crystal structure of $CeTe_3$ consisting of corrugated CeTe slabs, and Te layers, where Te atoms are separated by 3.1 Å in a square-net. The figure is courtesy of H.J. Kim.

4.2.2 CDW detection and revised structure of $CeTe_3$

In the initial crystallographic structural interpretation perfect square nets of Te atoms separated by ~ 3.1 Å were assumed. However, recent more careful studies involving electron diffraction, superstructure and super space group approaches revealed that this is only an average representation, and that the real structure is more complicated, containing distorted tellurium nets [90]. These experimental observations confirmed theoretical predictions of square net arrangements being unstable, and prone to CDW formation [92], as mentioned.

The existence of a unidirectional CDW in tritellurides was first detected in transmission electron microscopy study of series of $RETe_3$ by DiMasi and collaborators [89]. They identified superlattice reflections in the electron diffraction pattern corresponding to a single incommensurate modulation wave vector with a magnitude of q_{CDW}

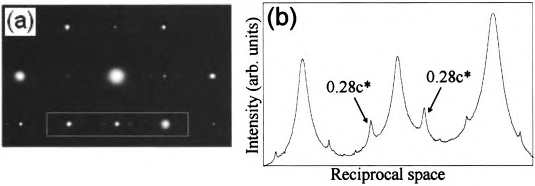

Figure 4.3: (a) Selected area electron diffraction pattern of $CeTe_3$, and (b) selected intensity scan along the c* direction of the electron diffraction pattern marked with a box in (a). The arrows indicate the positions of the observed superlattice reflections. The figure is courtesy of C. Malliakas [91].

$\approx 2/7 \times 2\pi/c$. This indicated the presence of incommensurate distortions in the Te layer planes. The incommensurate superstructure was solved within space group *Ama*2 for RE = Ce, Pr, and Nd by Malliakas and collaborators using single crystal x-ray diffraction [91]. Figure 4.3 shows the electron diffraction pattern of $CeTe_3$ featuring superlattice reflections. This study quantified distortions in the Te net, and revealed that a distribution of planar Te-Te distances exists, with a minimum value of ~ 2.95 Å and a maximum value of ~ 3.24 Å.

This was further qualitatively confirmed by means of the atomic pair distribution function (PDF) method, based on a total scattering approach, which gives structural information in direct space. A small shoulder (Figure 4.4) at ~ 2.9 Å is evident to the left of the principal PDF peak at around 3.1 Å, which is due to the short Te-Te bonds.

Further detailed local atomic structural study of Kim and co-workers [96] on $CeTe_3$ utilizing the PDF method showed that local atomic distortions of the Te nets due to the CDW are larger than those observed crystallographically [91]. Distinct short (2.83 Å) and long (3.36 Å) Te-Te bonds are found to be present in the structure, consistent with bimodal bondlength distribution. The discrepancy between the local and crystallographic model has been interpreted in terms of the discommensurated

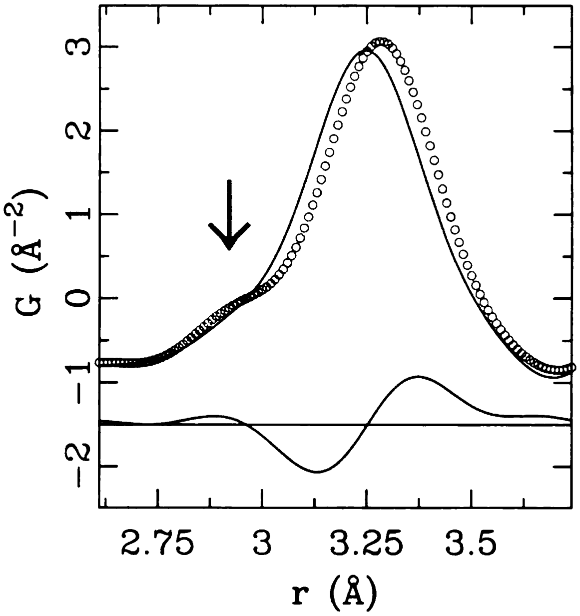

Figure 4.4: The experimental atomic PDF of $CeTe_3$ (symbols) up to 3.7 Å, featuring a shoulder that corresponds to ~ 2.9 Å Te-Te distance, indicated by the arrow. The solid line represents the *Cmcm* model that assumes an undistorted Te net, and the difference curve is offset below. This model clearly does not explain the data. The data are courtesy of H.J. Kim [91].

nature of the CDW in $CeTe_3$. While the PDF is sensitive to the local displacements within the commensurate regions, the crystallographic result provides the same information averaged over many discommensurated domains. The PDF study estimated the commensurate domain size to be about 27 Å [96].

4.3 Electronic properties of $RETe_3$

Due to the large lattice constant along the b-direction (~ 25 Å), as shown in Figure 4.2, the Brillouin zone of $RETe_3$ is squashed (plate-like) and slightly orthorhombic [104]. Strong anisotropy has been observed in their transport properties [89, 94]. For $CeTe_3$ this is shown in Figure 4.5, featuring low-temperature resistivity, as obtained by Ru and Fisher [94]. This reflects the nearly two-dimensional nature of the system originating from the weak hybridization between the Te layers and the RETe slabs. Electronic structure for tellurium planes is rather simple. The electronically

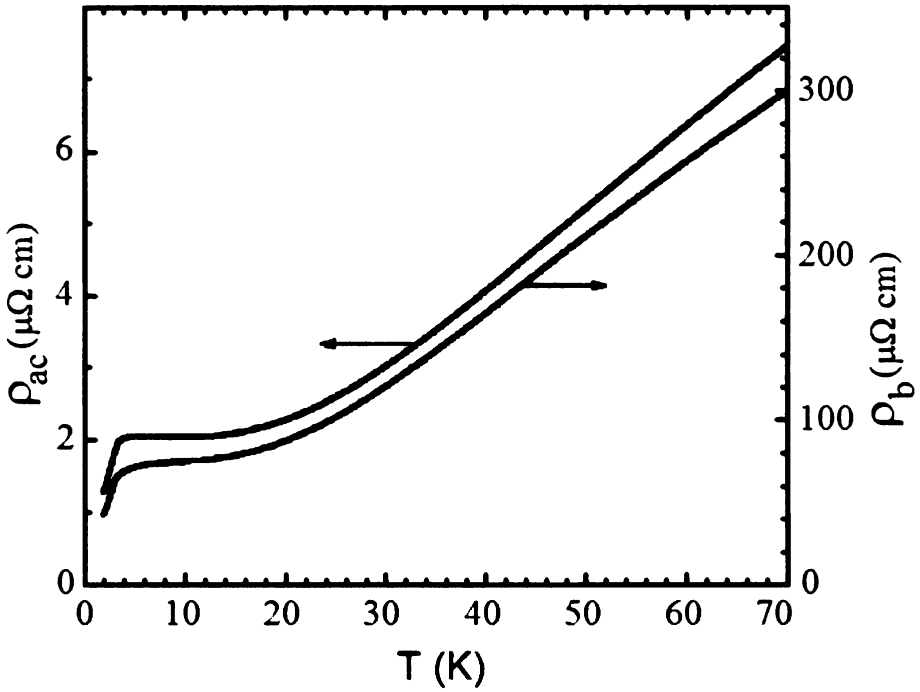

Figure 4.5: Low-T resistivity of $CeTe_3$, as obtained by Ru and Fisher [94], for current flowing within Te layers and along the direction perpendicular to it. Arrows indicate corresponding ordinates. Note the degree of anisotropy: at ~ 45 K the in-plane resistivity is about 50 times smaller than that corresponding to the out-of-plane direction.

active valence band consists predominantly of $5p$ orbitals of the Te atoms from the Te planes. The only significant role is played by the perpendicular chains of in-plane $5p_x$ and $5p_y$ orbitals, since the energy of completely filled $5p_z$ is pushed below the Fermi level as indicated by the first principle band structure calculations [105, 106].

After it was first detected in $RETe_3$ from TEM studies [89], the CDW state was also observed in this family of materials by other experimental techniques. More recently observation of a CDW in $CeTe_3$ was made by ^{125}Te NMR studies on single-crystal sample [107]. The NMR spectrum showed three split lines, an indication of spatial modulations of the magnetic shifts and the electric field gradients at Te nuclear positions, consistent with the presence of an incommensurate CDW.

ARPES, which is the most direct technique to visualize the dispersion of the

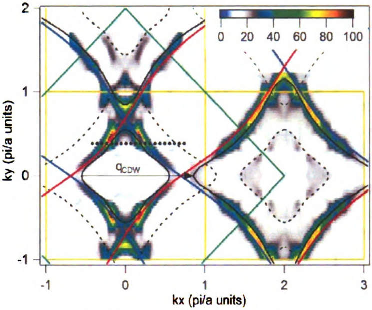

Figure 4.6: Contour plot in reciprocal space of ARPES spectral weight for $CeTe_3$ at 25 K, representing a Fermi energy intensity map, as obtained by Brouet and collaborators [95]. The arrow indicates characteristic nesting vector $\mathbf{q}_{CDW}$.

occupied bands, found a rather large CDW gap in the optimally nested regions of the Fermi surfaces of $SmTe_3$ ($\sim$ 280meV) [108] and of $CeTe_3$ ($\sim$ 400meV) [95, 104]. If these values are substituted in the mean-field calculations, transition temperatures to a CDW state are estimated to be around 1500-2000 K [109], values that are beyond the melting point of these materials. Large suppression of mean-field values is therefore expected and observed [109, 110]. In Figure 4.6 a Fermi energy intensity map of $CeTe_3$ at 25 K is shown [95], indicating that the CDW wave vector nests large portions of the Fermi surface. The Fermi surface is gapped, with the gap value as indicated. This strongly supports the idea that the CDW phenomenon is driven by Fermi surface nesting [108, 104, 95]. While optimally nested regions are gapped, the other sections of the Fermi surface with poorer nesting remain ungapped, which explains why the material shows metallic behavior in the CDW phase.

Accurate values of T_{CDW} are typically obtained from either detailed diffraction studies, where superlattice peak intensities corresponding to the CDW order are monitored in the diffraction patterns as a function of temperature, or from transport

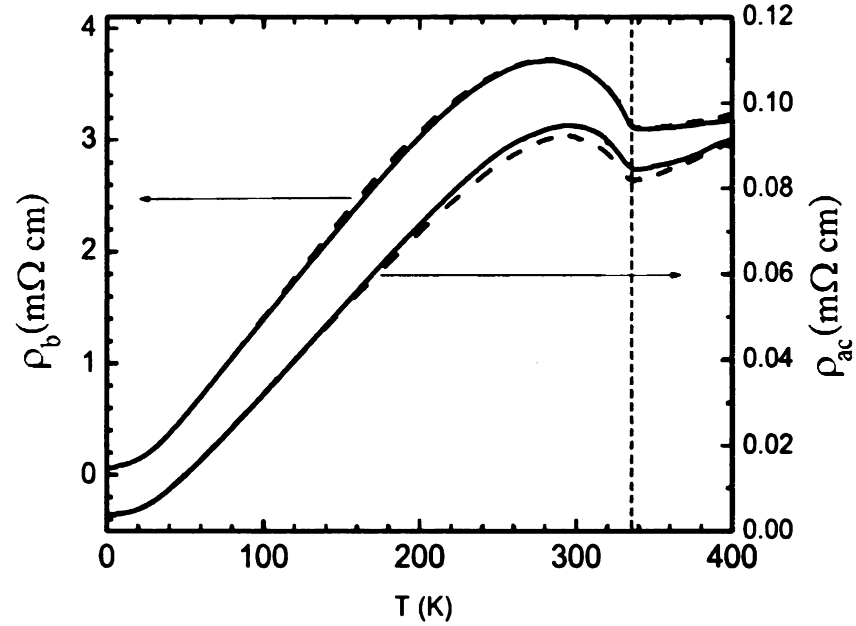

Figure 4.7: Temperature dependence of the anisotropic resistivity for $TbTe_3$, as measured by Ru and co-workers [110]. Arrows indicate corresponding ordinates for the in-plane and perpendicular directions. A characteristic change in resistivity is present around T_{CDW} = 336 K, as indicated by the vertical dashed line.

measurements where distinctive kinks are observed in the temperature-dependent data. For the $RETe_3$ family, T_{CDW} varies from about 240 K in $TmTe_3$ to values above 400 K in $SmTe_3$ and other members with lighter RE [110]. For $CeTe_3$ the transition temperature has not been determined to date, as transport measurements were carried out up to 400 K. Based on the mean-field predictions using measured values of the CDW band gap, that predicted T_{CDW} of 1600 K for $TbTe_3$ while the observed value was over 4 times smaller [109, 110], we can use the mean-field T_{CDW} value of over 2000 K for $CeTe_3$ and project the expected measured value to be above 500 K. Due to the lack of transport data for $CeTe_3$ that show the CDW transition, I show the temperature dependence of $TbTe_3$ resistivity, Figure 4.7, as obtained by Ru and collaborators [110]. Again we see highly anisotropic transport properties, as expected, and we also see a distinct change in resistivity at the transition temperature which is indicated by the vertical dashed line. Interestingly, the kink is present

RETe$_3$	$q_{CDW}/(2\pi/c)$ **at 300K**	**CDW gap (meV)**	**T$_{CDW}$ (K)**
CeTe$_3$	0.2801	400	> 500
NdTe$_3$	0.2827	-	> 450
SmTe$_3$	0.2874	280	415
TbTe$_3$	0.2957	240	336
TmTe$_3$	N/O	-	240

Table 4.1: Characteristics of some of the rare-earth tritellurides. The table shows q_{CDW} component, approximate maximum size of the CDW gap, and the CDW transition temperature. q_{CDW} components were measured by C. Malliakas. CDW gap values are based on ARPES measurements [95, 108]. CDW transition temperature values are based on resistivity measurements [110].

in both in-plane and out-of-the-plane resistivity curves, suggesting that the coupling between the layers may be stronger than originally thought. Another possible explanation may be that the out-of-plane resistivity is highly correlated with the electronic state of the planes containing Te nets.

Several CDW-related properties of some of RETe$_3$ (RE = Ce, Nd, Sm, Tb, Tm) that are known at present are summarized in Table 4.1.

4.4 Sample synthesis and experimental details

Single crystals of CeTe$_3$ are prepared by a halide flux method. Stoichiometric amounts of cerium ($\sim$ 0.3 g) and tellurium (0.82 g) were loaded into quartz tubes under nitrogen together with a double amount ($\sim$ 2 g) of halide flux (0.42:0.58 molar mixtures of RbCl and LiCl). All manipulations were carried out under dry nitrogen atmosphere in a Vacuum Atmospheres Dri-Lab glovebox. The tubes were sealed under vacuum ($<10^{-4}$ torr) and heated to 650 °C over 12 hours and kept there for 6 days. The tubes were then cooled down to room temperature at a rate of 4 °C per minute. The halide flux was dissolved in water and the crystals were washed with acetone and dried under nitrogen environment. The morphology of the crystals is that of thin plates with a brown (copper-like) color. Electron microprobe energy dispersive spectroscopy (EDS) was performed on several crystals of the compound and confirmed the 1:3 ratio of the cerium to tellurium and the absence of other elements of the flux. The compound is found to be x-ray pure and moisture sensitive after exposure to air for a few days. The single crystal samples were prepared and characterized by C. Malliakas. Other samples used in this study were prepared using similar synthesis routes.

STM experiments were performed on several single crystals of $\mathrm{CeTe_3}$. The crystals were carefully prepared by cleaving them with an adhesive tape so that the exposed layers were tightly packed without loose flakes. The cleaved crystals were about 2x2 mm in size, and with thickness of approximately 200 μm. The measurements were carried out at 300 K and 77 K in the constant current mode of STM and in the STS mode. Data were acquired with a bias voltage of 100 mV and with a tunneling current of 0.6 nA. The experimental data were analyzed in both direct and reciprocal space. Fourier transforms (FT) of the STM images were generated using commercially available image analysis and processing software for nano- and micro scale microscopy, "Scanning Probe Image Processor (SPIP)" [111].

In the experiments carried out in this study, slow drift effects tended to shift the apparent position of the atoms after several scans. Therefore, simple averaging of many scans did not always improve the signal to noise ratio in the data. With this is mind, we processed our data using the following approach: a set of multiple STM images were averaged together, after which the Fourier transform from the average was obtained. This procedure was then repeated several more times for the next sets of images. As phase information is not included in the FT image, we eliminated the drift effects that could otherwise obscure the results.

4.5 Results of STM measurements on $CeTe_3$

4.5.1 Room temperature data and the nature of the CDW

Initial STM experiments on the exposed Te net of a freshly cleaved single crystal of $CeTe_3$ were performed at 300 K. These measurements have successfully resolved the CDW. A real-space STM image, showing both the atoms of the Te net (dark yellow features) and the CDW modulations (bright yellow features) oriented at $\sim 45°$ to the net, is shown in Figure 4.8. The areas of low intensity correspond to interatomic spacing. On the expanded image the network of Te distances is superimposed as a guide to the eyes. This image represents a first direct observation of CDW in $CeTe_3$, and is a result of the average of eight images that were obtained consecutively at a scan range of 27 nm x 27 nm. This was the maximum scan range used that was still providing images with atomic resolution. Moreover, the images shown in Figure 4.8 were Fourier filtered to eliminate the angstrom-scale scatter artifacts and obtain a clearer image. This procedure was carried out by Fourier transforming the raw data to reciprocal space, eliminating the longest wave-vector component that corresponds to the shortest wavelength features in the real space, and then back Fourier transforming the data, resulting in the image shown in Figure 4.8. This filtering process is routinely performed on STM images spanning wide range that involve large numbers of atoms. I direct interested readers to inspect for comparison the 77 K data image (Figure 4.12) where this procedure was not carried out.

Results of the atomic PDF method based on x-ray experiments showed that there is a bimodal bond-length distribution in Te nets with distinct short and long Te-Te bonds in the structure, as detailed in Section 4.2.2 [96]. Such bimodal bond-length distribution indicates the commensurate CDW. In case of a uniformly incommensurate CDW, the Te-Te bondlength distribution is expected to be Gaussian, which was not observed experimentally in the local structure. Since it is known that CDW

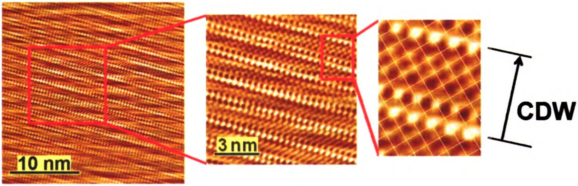

Figure 4.8: (This figure is presented in color.) A representative room temperature STM image of the Te net, showing both Te atoms and the CDW modulations oriented at 45° to the net. The image, obtained at a scan range of 27 nm x 27 nm, has been Fourier filtered. On the expanded image, the network of Te distances is superimposed. Lines indicate locations of high charge density due to the CDW, while the arrow marks the CDW direction.

modulation is incommensurate on average, this may indicate that the structure consists of commensurate domains separated by discommensurations. The PDF analysis involving variable r-ranges showed that as the distance range in the PDF refinements is increased, the bimodal distribution crosses over to the crystallographic distribution (Gaussian like) at around 27 Å. This defines the characteristic lengthscale in this interpretation for commensurate domains as seen by the PDF method.

Since the STM is also a local probe, we sought an analysis method of STM data to address this important issue. It should be noted that the CDW displacements are typically rather small; the atomic displacements are about 5 % of the interatomic spacing, while the conduction electron density varies by several percent. While such small atomic displacements cannot be noticed from the STM image by naked eye, the density variations are easily observed in the real space. Further, analyses of the real-space STM images are inadequate to distinguish between locally commensurate states with discommensurations and uniformly incommensurate states [112]. Fortunately, it has been shown that one possible method for determining the nature of the CDW system from STM experiments is to examine the Fourier transform of the STM images. As demonstrated by Thompson and coworkers, satellite peaks in the FT of the STM images observed in the vicinity of the principal CDW peaks, represent direct experimental evidence of discommensurations and domain structure in 1T-TaS$_2$ [113]. Moreover, from the Fourier transform of STM images, one can estimate the characteristic size of the domains through analysis of the wave vectors.

Here I provide a summary explaining the origin and significance of satellite peaks in the FT of STM data. In the case of 1D discommensurate CDWs, the wavefunction of the CDW can be written as the product of a uniformly incommensurate CDW and a modulation envelope [114],

$$\psi_{CDW}(x) = \psi_{IC}(x)M(x). \tag{4.1}$$

Function

$$\psi_{IC}(x) = \psi_0 exp(ik_{IC}x) \tag{4.2}$$

is the wavefunction of the uniformly incommensurate CDW, where k_{IC} is the incommensurate wave vector and $M(x)$ is a modulation envelope. Assuming that the modulation envelope is periodic with periodicity $\lambda=2\pi/k_D$, we can express it as a Fourier series in the modulation wave vector k_D

$$M(x) = \sum_n f_n exp(ink_D x). \tag{4.3}$$

The first two terms in modulation envelope are important since they are much larger than the higher-order terms. Thus equation

$$\psi_{CDW}(x) = f_0\psi_{IC}(x) + f_1\psi_{IC}(x)exp(ik_D x) + ... \tag{4.4}$$

has terms in the Fourier expansion at k_{IC} and at $k_{IC} \pm k_D$. The term at k_{IC} is the fundamental incommensurate CDW peak in FT, and terms at $k_{IC} \pm k_D$ are the satellite peaks which are the signature of modulation due to the domain structure [113].

Hence the difference in wave vectors of the main peak and the corresponding satellite provides information about the domain size. We can understand this as a beating pattern of two waves with nearly the same wave vector. For example, closely spaced wave vectors k_1 and k_2 result in beats with wave vector $k = k_1 - k_2$. With respect to this discussion, the separation in k-space is k_D, which corresponds to a wavelength for the beating pattern of $\lambda = 2\pi/k_D$. These ideas can be applied directly to STM data to characterize the nature of CDW and its relationship to the lattice.

The corresponding two-dimensional FT of the raw STM data collected at 300 K, is shown in Figure 4.9. This FT image represents information from a total of 24 STM images, and is obtained by averaging three FTs of the STM images that are themselves averages of eight scans. The unprocessed transform image shows enhanced noise along the vertical axis, which is an experimental artifact due to the scan direction, that was setting a color scale of the FT image in such a way that all the features of interest close to the origin were hard to see. To better see the peaks near the origin, we applied a line-by-line correction to remove this noise. This creates the dark line along the y axis, as seen in Figure 4.9. Horizontal and vertical axes are wave vector components k_x and k_y. The peaks are labeled for easier identification.

The square Te net gives rise to four distinct peaks (L). Peaks at 45° to the Te net are along the direction where we expect to see the CDW peaks. The direction of the CDW is indicated by the arrow. We now identify the peaks of interest for the analysis, where all labels refer to these in Figure 4.9. The fundamental CDW peak (nesting vector with magnitude $q_{CDW} \approx 2/7 \times 2\pi/c$) [89] and the first harmonic $\lambda/2$ are labeled 1 and 3, respectively. We think that peak 5 corresponds to the underlying Ce atoms, which form a square lattice below the surface oriented at 45° to the Te-net, i.e., along the CDW direction. Hence we conclude that, under the conditions of this measurement, the surface Te atoms and subsurface Ce atoms have comparable

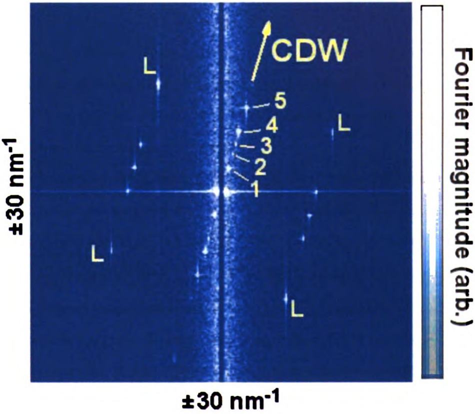

Figure 4.9: (This figure is presented in color.) The two-dimensional Fourier transform of the room temperature STM data. The unprocessed transform image shows enhanced noise along the vertical axis, an artifact due to the scan direction. To better resolve the peaks near the origin, we applied a line-by-line correction to remove this noise. This creates the dark line along the y axis. Horizontal and vertical axes are wave vector components k_x and k_y. The square Te net gives rise to four distinct peaks (L). Peaks related to the CDW are oriented at 45° to Te net peaks, as indicated by the arrow. The fundamental CDW peak and the first harmonic are labeled 1 and 3, respectively. Peaks 2 and 4 are in close proximity to peak 3, and peak 5 corresponds to the underlying structure.

tunneling matrix elements. It is likely that the Ce f-electrons hybridize with Te conduction states (with large amplitude at the surface) giving rise to a density of states enhancement near the Fermi level [115]. This is further supported by the results of a simulation of STM image shown in Figure 4.10. STM results were simulated using electronic structure calculations based on density functional theory [116, 117, 118, 119]. The image is obtained from calculations in a slab geometry by calculating the charge density in an energy range 0.05-0.1 eV at a plane 3 Å above the surface Te atoms. The simulation shows that the subsurface Ce atoms should contribute significantly to the surface tunneling signal.

Peak 4 is separated from peak 5 by the fundamental CDW wave vector, the magnitude of which corresponds to the position of peak 1. This indicates that the subsurface lattice is also distorted by the CDW. Following the work of Thomson *et al.* (Ref. [113]) a satellite peak needs to be identified in order to establish if the CDW is in a discommensurated state. The only peak along the CDW direction that remains unidentified is peak 2. Since this peak is in close proximity to peak 3, and based on the discussion given above, it could be interpreted as a satellite to peak 3. This is then supporting the idea that the CDW in the Te-net is discommensurated. The characteristic size of the commensurate domains, or the distance between discommensurations, can then be estimated from the differences in the wave vectors k_D, as described above. From the separation of peaks 2 and 3, we find a characteristic domain size of $\lambda = 2\pi/k_D \approx 38(2)$ Å.

However, there are some concerns with this interpretation. In general, based on Eq. 4.4, one would expect peak 3, at around 7.5 nm^{-1}, to have *two* satellites at $k_{IC} \pm k_D$, the first satellite being peak 2 at 6.0 nm^{-1}. Indeed, our data show peak 4 in close proximity to peak 3, to the right of it, but this peak is *not* at the correct position in order to be considered as a second satellite to peak 3, equivalent to the satellite peak 2. This is shown explicitly in Figure 4.11. Figure 4.11(a) shows a line

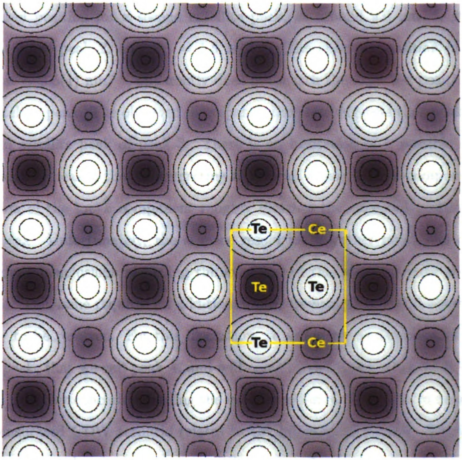

Figure 4.10: Simulated STM image of $CeTe_3$ from theoretical calculations. The image is simulated by calculating the charge density in the plane 3 Å above the surface Te layer, obtained for an energy range between 0.05 eV and 0.1 eV above the Fermi level. The first atomic layer below the surface Te layer is Ce layer. The color scale denotes charge density changes: light color denotes large charge density, while dark color denotes small charge density. The square marks one unit cell along the *a* and *c* directions, with a lattice parameter of 4.4 Å. Simulation courtesy of Z. Rak.

cut of the data from the Fourier transform Figure 4.9 taken along the direction of the CDW. The line cut starts from the origin, and goes through the peaks in the CDW direction. Figure 4.11(b) shows the same data on an expanded scale, focusing on peaks 2, 3, and 4, to better determine the peak positions. The red arrow indicates the expected position for a second satellite peak, at around 9.0 nm^{-1}, given our interpretation of peak 2, and $k_D = 1.5$ nm^{-1}. The observed position of peak 4, however, at $\sim 9.5(1)$ nm^{-1}, apparently does not match the expected position of the second satellite peak. The observed discrepancy therefore suggests that peak 4 is *not* the second satellite peak of peak 3. There is an indication of a possible shoulder at low-k side of peak 4 that is suggesting that peak 4 may be two-component, and the position of the low-k component roughly matches the expected position of the satellite peak. Unfortunately, the k-space resolution is rather poor, and does not allow to draw conclusions regarding the existence of this shoulder peak with great confidence. This issue requires an additional measurement that would allow for this ambiguity to be resolved. For this discussion we are going to assume that there is only one peak, that we call peak 4, and will come to this again when 77 K data are discussed. Another concern regarding the interpretation of the results in terms of the discommensurated CDW scenario relates to the intensity of peak 4. The intensity of peak 4, if considered as a satellite peak to the CDW peak, is actually greater than the intensity of the CDW peak itself, while we expect satellite peaks to have always smaller intensity than the principal peak. In addition, it can be noted that the fundamental CDW peak is lacking its satellites, which were considered in the original work of Thomson and co-workers to estimate the commensurate domain size. This leads to a conclusion that our hypothesis about the nature of peak 2 should be re-examined.

Another possibility, within Thomson's interpretation, is to consider peak 2 as a satellite to the principal CDW peak 1. In such case, the second satellite of peak 1

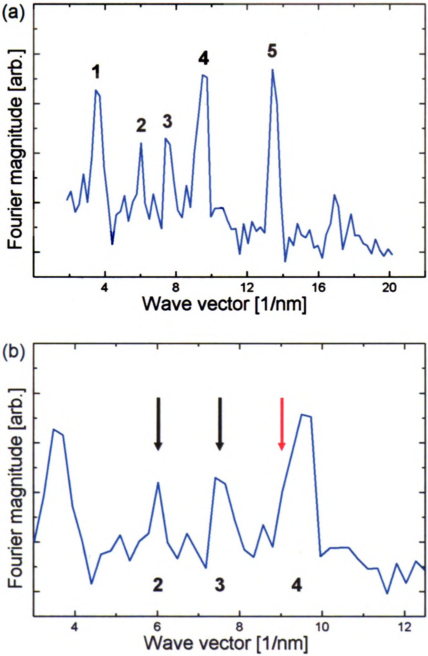

Figure 4.11: (This figure is presented in color.) Part (a) shows a line cut of the data from Figure 4.9 starting from the origin in the direction of the CDW. Part (b) shows the same data with an expanded scale. The red arrow indicates where we would expect to find a 2^{nd} satellite peak, given our interpretation of peak 2 (as a satellite peak).

would be positioned to its left, toward the origin in Figure 4.11. This is not observed due to enhanced noise near the origin. The satellite peaks of the first harmonic, peak 3, are in this view not observed as these would be sufficiently small and buried in the background. An estimate of commensurate domain size can then be made based on the difference between the positions in peaks 2 and 1, which is about $k_D =$ 2.5(2) nm^{-1}. This yields a characteristic domain size of $\lambda=2\pi/k_D \approx 25(2)$ Å. This is then much closer to the value obtained from PDF analysis than the estimate using peak 2 as a satellite to peak 3. However, this interpretation has no explanation for peak 4, which is one of the most prominent features.

4.5.2 Results of STM at 77 K

Here I present results of scanning tunneling microscopy measurements of the $\mathrm{CeTe_3}$ surface obtained at 77 K temperature. Compared to the room temperature measurements [96] where, due to drift effects, data were noisier, measurements at 77 K provide data of better quality. The peaks in the Fourier transform of the real-space data obtained at 77 K are sharper allowing for the new analyses. A representative atomic resolution real-space STM image is shown in Figure 4.12. In some sections of the image the complete net of Te atoms is clearly visible, while in other sections only every other atom appears brighter. CDW modulation is oriented at 45° to the Te net, as in room temperature data.

Analysis of the Fourier transform of the real space data was performed in the same way as for the room temperature data. Figure 4.13 shows a Fourier transform of the 77 K temperature real-space data obtained at a scan range of 24 nm x 24 nm. The FT image contains information from a total of 16 STM images, by averaging four FTs of the STM images that are averages of four scans each. The Te square lattice peaks are labeled L. Peaks related to the CDW are oriented at 45° to the square lattice peaks. In order to resolve peak positions we again take a line cut along the CDW direction

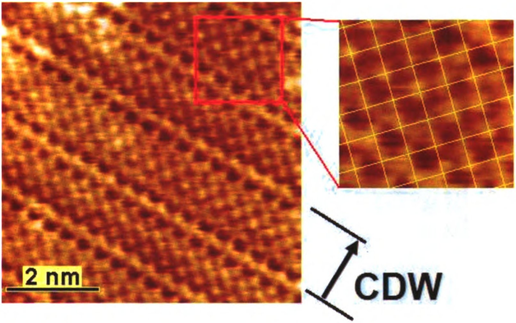

Figure 4.12: (This figure is presented in color.) A real-space STM image of the Te net obtained at 77 K, showing both Te atoms and CDW modulations oriented at 45° to the net. The image is the average of four images that were obtained consecutively at a scan range of 10.2 nm x 10.2 nm, with just a line-by-line correction. Here we show the biggest area without substantial contamination, although some contamination is present as seen in the upper left corner. The approximate size of the displayed area is 6.5 nm x 6.5 nm. Lines indicate locations of high charge density due to CDW, while the arrow marks the CDW direction.

in Figure 4.14. The CDW peak $q_{CDW} \approx 2/7 \times 2\pi/c$, where $c=\sqrt{2}a$ and a is the Te-Te separation of 3.1 Å, at around 3.9 nm^{-1} is the first prominent peak, as labeled. Peak q, at 14.3 nm^{-1}, corresponds to the underlying structure closest to the surface, in this case the Ce atoms, which form a square lattice below the surface oriented at 45° to the Te-net. Again, as in the room temperature case, four additional peaks can be clearly observed. The data are of better quality and less noisy than that obtained at room temperature.

The first observation we make is that the peak corresponding to peak 4 in the linecut along the CDW direction of the room temperature data (Figure 4.11) this time does *not* contain a shoulder at low-k side. This removes the ambiguity that was present in the room temperature data.

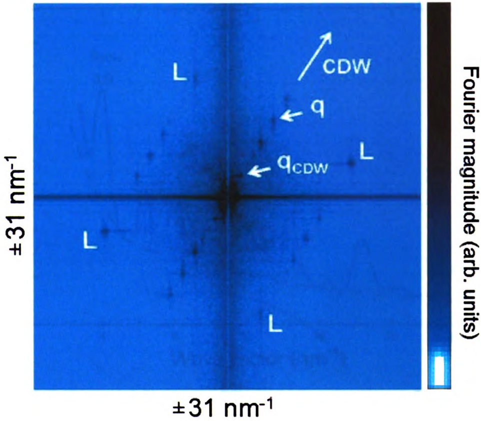

Figure 4.13: (This figure is presented in color.) The Fourier transform of the low temperature STM data. Enhanced noise along the vertical axis is an artifact due to the scan direction. Horizontal and vertical axes are wave vector components k_x and k_y. The square Te net gives rise to four distinct peaks (L). Peaks at 45° to Te net are consistent with the CDW peaks. The CDW peak q_{CDW}, as well as peak q related to underlying Ce atoms, are labeled.

4.5.3 Wave vector mixing

Observation of satellite peaks in the vicinity of the principal CDW peak in the FT of the STM data, as discussed earlier, would be evidence of a discommensurated CDW. However, it is hard to unambiguously establish if the extra peaks observed in the FT of the STM data are indeed satellite peaks. We shall, therefore, explore another origin of the peaks observed in the FT. In real-space images it is not uncommon to observe contributions to the STM signal due to the subsurface layer, and measurement conditions, such as the exact configuration of the STM tip can

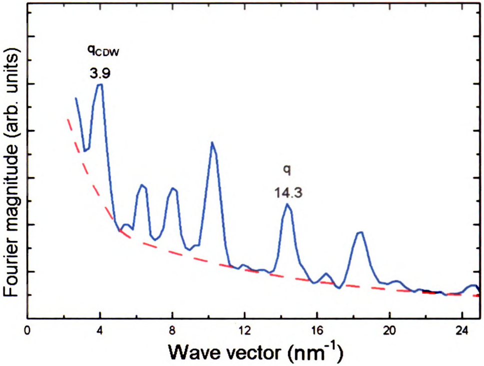

Figure 4.14: (This figure is presented in color.) Subset of the data from the Fourier transform along a path from the origin in the direction of the CDW. Noise in the Fourier transform becomes significantly larger near the origin. This is due to the impurities present in the real-space data. As the guide to the eye, the red dashed line indicates the background noise.

lead to non-sinusoidal atomic signals. In the case of a uniformly incommensurate CDW, ideally it is expected to give only two peaks in the FT of the STM data in the CDW direction, one corresponding to the incommensurate CDW, and the other due to the underlying lattice. In real space this corresponds to a superposition of two sinusoidal signals. However, if appreciable non-sinusoidal components are present, then the two waves may resemble a product, as illustrated in Figure 4.15. Algebraically, the product of two sine waves can be expressed as a sum and a difference: $\sin(A)\sin(B) = \frac{1}{2}\cos(A-B) - \frac{1}{2}\cos(A+B)$. This effect can lead to extra peaks in the Fourier transform. In order to demonstrate this, we carried out a series of simulations to mimic the effect of non-sinusoidal artifacts and explore the effect that this has on the FT of the real space image. We start from an undistorted superposition

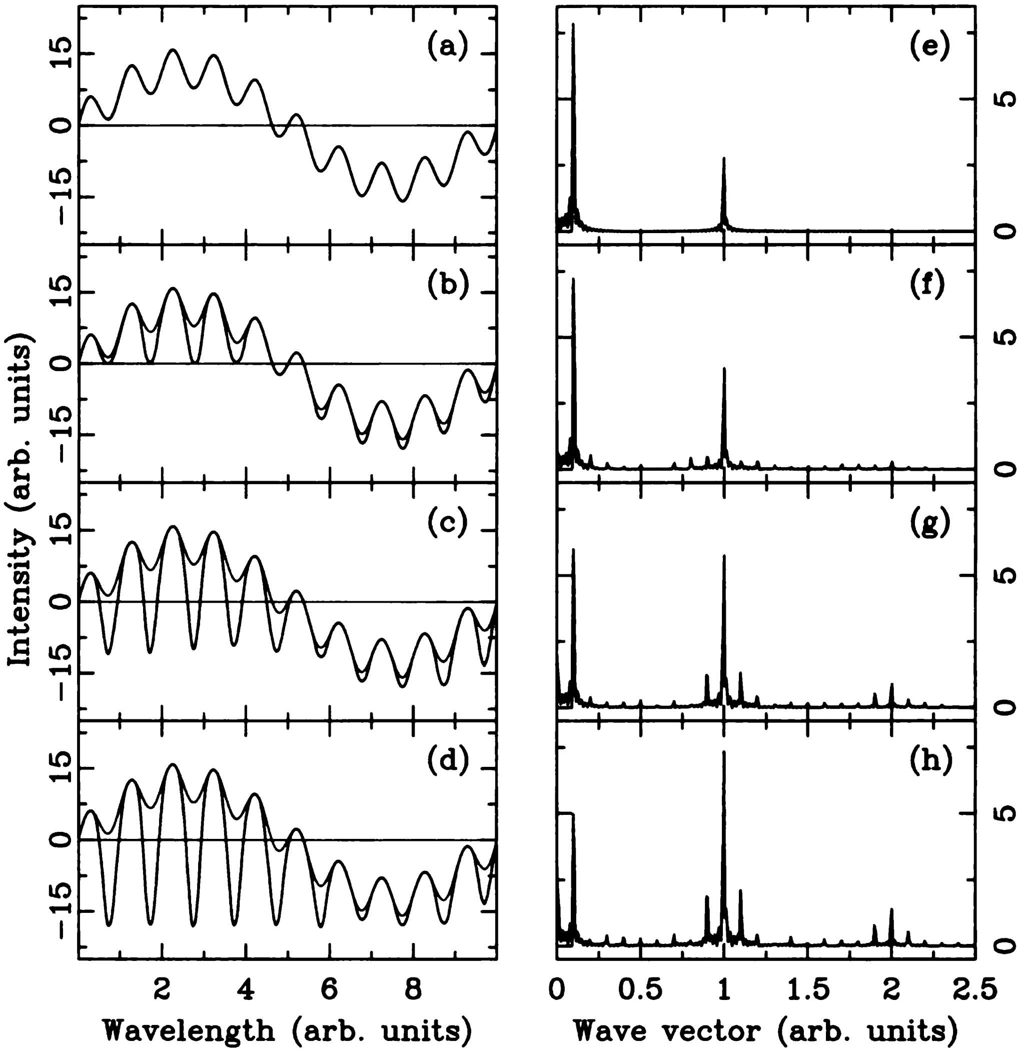

Figure 4.15: (a) Simulated one-dimensional STM signal representing the superposition of two sine waves: the short wavelength represents lattice effects, while the long wavelength represents CDW. The corresponding Fourier transform is shown in panel (e). Non-sinusoidal distortions to the simulated STM signal of various magnitudes were considered in (b)-(d), with the original signal shown as a gray curve for comparison. The corresponding Fourier transforms are given in panels (f)-(h). Additional peaks appear at special positions in the Fourier transform as the distortion is introduced. See text for details.

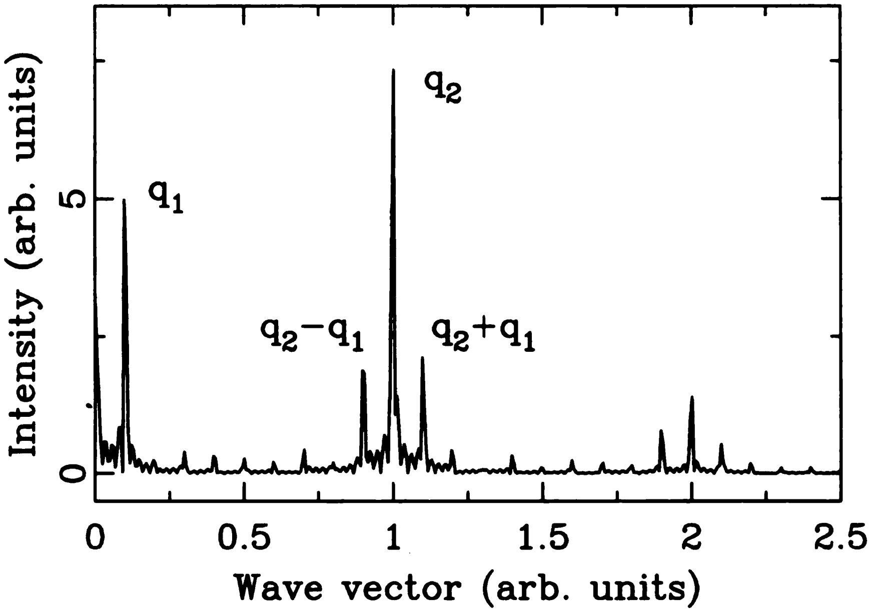

Figure 4.16: Fourier transform of the distorted signal from Figure 4.15(h). While in the Fourier transform of undistorted signal only peaks labeled with q_1 and q_2 appear, as they correspond to the two superposed waves in the direct space, additional peaks are observed in the case when distortions are present. These additional peaks occur at q_2-q_1, q_2+q_1, $2q_2$, $2q_2$-q_1, $2q_2$+q_1, and other linear combinations.

of two sinusoidal signals, one with large and another with small wavelength, λ_1 and λ_2, respectively, representing the CDW and the underlying lattice, Figure 4.15(a). The Fourier transform of this superposition consists of two peaks at positions $q_1 = 2\pi/\lambda_1$ and $q_2 = 2\pi/\lambda_2$, as shown in Figure 4.15(e), that represent the two Fourier components in this Fourier decomposition. A series of distortions with various magnitudes is then introduced to the superposition, to observe their effect on the Fourier transform. These distorted signals are shown in Figure 4.15(b)-(d), with the undistorted signal superimposed for comparison (gray curve). The corresponding Fourier transforms, shown in Figure 4.15(f)-(h), contain additional peaks that appear at special positions, and which originate from the distortions that are introduced to the original signal. These additional peaks, reproduced for clarity in Figure 4.16, occur at positions corresponding to various linear combinations of q_1 and q_2, such as q_2-q_1 and q_2+q_1, where q_1 and q_2 are the Fourier components of the original undistorted

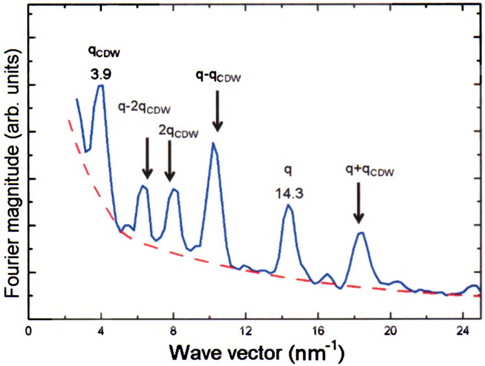

Figure 4.17: (This figure is presented in color.) Subset of the data from Fourier transform along path from the origin in the direction of the CDW. Noise in the Fourier transform becomes significantly larger near the origin. This is due to the impurities present in the real-space data. As the guide to the eye, the red dashed line indicates the background noise.

signal.

Having this in mind, the interpretation of additional peaks in the FT of our STM data on $CeTe_3$, shown in Figure 4.14, can then be given as follows. In the case of ideal STM measurements and a uniformly incommensurate CDW we expect to observe only peaks at q and at q_{CDW} along the CDW direction, coming from the periodicity of underlying structure below the surface and from the CDW periodicity, respectively. Due to the distortion effects in the STM measurements, wave vector mixing is present and the additional peaks occur, as shown in Figure 4.17. They are a linear combination of the CDW wave vector q_{CDW}, and the wave vector q. In the figure, the peaks are labeled in the increasing order as follows: $q\text{-}2q_{CDW}$, $2q_{CDW}$, $q\text{-}q_{CDW}$, $q\text{+}q_{CDW}$. This analysis is similar to analysis given by Fang *et al.* to explain the FT of the STM data of $TbTe_3$ [97]. An important difference between the analysis of Fang and the one presented in this work is that we identify the first peak as the CDW wave vector, whereas Fang and co-workers use equivalent wave vector corresponding to $q_{CDW} \approx 5/7 \times 2\pi/c$. As a result, subsequent structure in our case can be explained well without invoking unresolved wave vectors, while Fang *et al.* invoked wave vector 2q corresponding to a wavelength which is even shorter than the lattice spacing. In this view, the STM data of $CeTe_3$ can be seen as consistent with a uniformly incommensurate CDW.

4.6 Scanning tunneling spectroscopy of $CeTe_3$

Formation of the CDW state in a material, as described in section 3.2.1, is associated with an energy gap opening up at the Fermi level. Using the point spectroscopy mode we can probe the CDW gap at different locations of the sample surface and estimate its size. STS measurements on $CeTe_3$ were performed at a temperature of 77 K at various locations of the tip above the surface of the exposed Te plane. Sweeping the bias voltage V in ranges of ± 300 mV and ± 400 mV, we have measured the tunneling current I as a function of the voltage. Differentiation of $I(V)$ data with respect to V gives the local density of states (DOS), as has been explained in the Scanning Tunneling Spectroscopy Section 2.2.2. The determination of the gap size from STS measurements is often hard due to the presence of the subgap states. In this work, under such circumstances, the gap has been determined by linear extrapolation of the STS signal before it changes slope due to the subgap states. The assigned size of the gap is then the approximate value obtained between the two intercepts of extrapolated lines with the zero dI/dV base line.

Curves of different shapes are obtained for the local density of states in spectroscopic measurements at different positions of the Te plane, indicating the local nature of the measurement. Here I show representative spectra of two kinds, one obtained

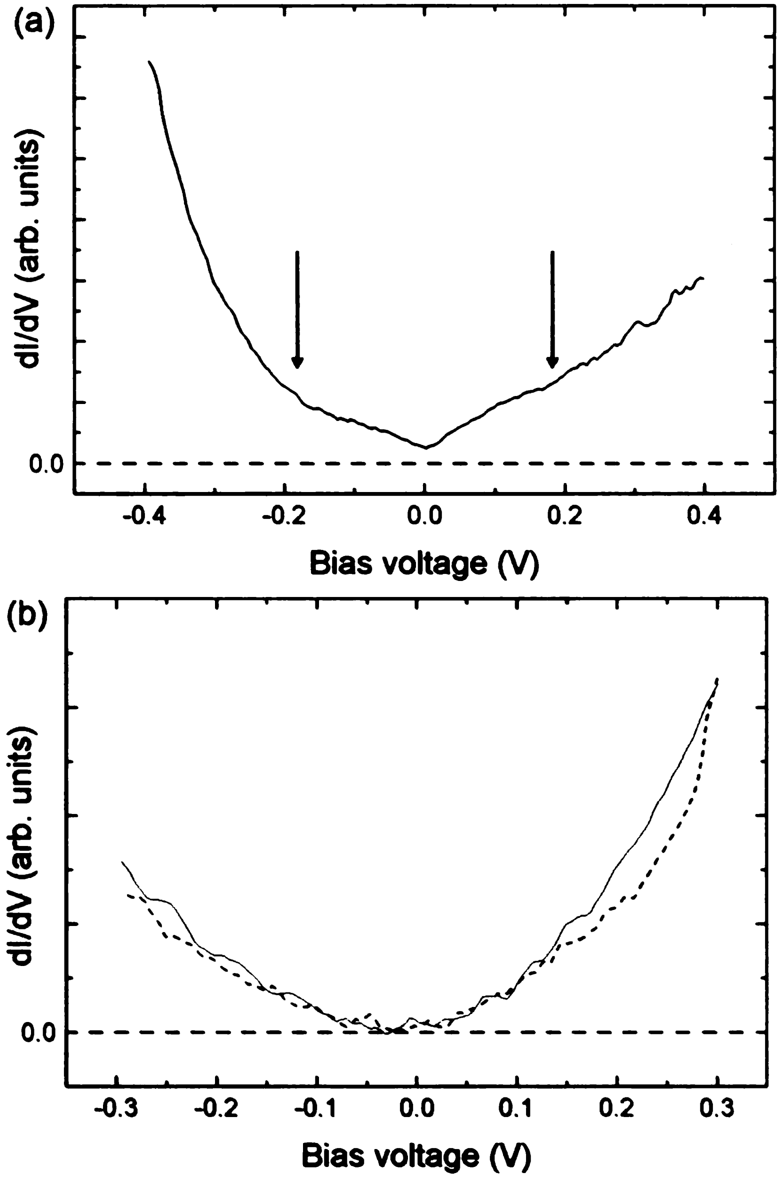

Figure 4.18: Local DOS around the Fermi level for $CeTe_3$. The Fermi level corresponds to zero bias voltage. The estimated CDW gap size in $CeTe_3$ is about 360 meV, as indicated by vertical arrows. The spectroscopy was carried out when the tip was located directly above a Te atom (a), and when the tip position was above the center of a Te plaquette (b). In the later case the data were collected above two adjacent plaquettes, shown as two curves, one above Ce and another above Te subsurface atoms. See text for details.

with the tip positioned directly above a Te atom, and another with the tip position between Te atoms, in the center of the plaquette consisting of four Te atoms. Figure 4.18(a) shows the characteristic density of states as obtained when the tip is at the top of a Te atom. The data represent an average of 168 measurements performed over the same spot consecutively. The Fermi level corresponds to zero bias voltage. From these data the value of the CDW gap is estimated to be 360 meV, in good agreement with the ARPES results [95]. The effect of thermal smearing of the data is approximately 3.5 $k_B T \approx 25$ meV at 77 K temperature. The local density of states has a shape that is suggestive of subgap states. This is characterized by an enhanced density of states when going towards the edges of both conduction and valence bands. There is noticeable asymmetry in the density of states in the conduction band (right from the Fermi level) and valence band (left from the Fermi level), with steeper rise in the valence band. The characteristic spectra obtained for the tip above the center of the Te plaquette is shown in Figure 4.18(b), for two adjacent plaquettes, one centered above Te subsurface atom, and another centered above Ce subsurface atom, therefore sampling different subsurface atoms. The data are averages of 69 and 15 measurements respectively, performed over the same spots consecutively. In this case, there is opposite asymmetry in the density of states in the conduction and valence bands, with a steeper rise in conduction band. We speculate that the solid line data in Figure 4.18(b) correspond to the STS measurement carried out over a plaquette centered above a Ce atom, where $4f$ states of Ce atom contribute to the density of states in the conduction band, giving rise to an apparent increase of DOS in that region. If this is the case, then the dashed line data correspond to the case of a plaquette centered above a Te atom.

It is expected that the tip location will affect the outcome of the measurement simply because areas with different spatial distribution of electronic density are probed for these different tip positions. However, the exact reason for the change of the shape of the density of states is still not fully understood. Our STS measurements suggest that there are contributions to the observed DOS that originate from one layer below the probed Te layer, most probably when the subsurface atom is Ce. However, more work is required to better understand, both qualitatively and quantitatively, the exact origin of the observed effects. Theoretical calculations exploring the local electronic band structure of $CeTe_3$ are being conducted in collaboration with Z. Rak and Dr. Mahanti to better understand this system [116]. By comparing our measurements to these calculations, we hope to get a complete picture of the local electronic structure.

4.7 STM and STS measurements on other $RETe_3$

We have attempted measurements on two other members of the $RETe_3$ family of materials, particularly YTe_3 and $GdTe_3$. Here I provide a brief summary of these attempts. Measurements on both materials were done at room temperature. Experiments on $GdTe_3$ were not successful, as we were not able to obtain the STM data with atomic resolution.

Measurements on YTe_3 were done in STM and STS modes, and the results are as follows. The STM measurements were of sufficiently good quality to allow for the atoms in the Te plane to be seen, but unfortunately the CDW was barely observed. We believe these problems originate from a slightly more chemically reactive surface.

Figure 4.19(a) shows one of the STM data sets obtained at the scan range of 5.2 nm × 5.1 nm, with bias voltage of 100 mV and tunneling current of 0.6 nA. Streaky features that are originating from the noise in the data are clearly visible, particularly at the top of the scan. For comparison I refer to Figure 4.8 and Figure 4.12, STM images of $CeTe_3$, that are of much better quality.

Figure 4.19(b) shows the Fourier transform of the STM data obtained at 8.4 nm × 8.1 nm, with bias voltage of 100 mV and tunneling current of 0.6 nA. Due to the bad

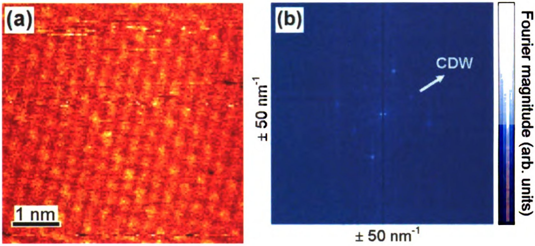

Figure 4.19: (This figure is presented in color.) (a) STM real-space image and (b) Fourier transform of YTe_3. STM data are obtained at the scan range of 5.2 nm × 5.1 nm, with bias voltage of 100 mV and tunneling current of 0.6 nA. The Fourier transform shown is that of the STM data with scan range 8.4 nm × 8.1 nm, obtained at bias voltage of 100 mV and tunneling current of 0.6 nA. These data are of poor quality, hence no conclusions related to the CDWs could be made.

quality of the STM data, the peaks in the CDW direction in the Fourier transform, which are of our interest, are insufficiently resolved and cannot be analyzed. For comparison, better quality Fourier transforms were obtained for $CeTe_3$, as shown earlier in Figure 4.9 and Figure 4.13. The results of the STM measurements of YTe_3 at room temperature are consistent with the presence of CDW in the system, as CDW-like features are observed in the scans. However, due to poor data quality no further conclusions could be drawn.

Spectroscopic test measurements of the CDW gap in YTe_3 were also carried out at room temperature. These measurements were partially successful, but the measurements were again prone to noise. In Figure 4.20 a representative local density of states curve obtained from these measurements is shown. Local DOS around the Fermi level clearly shows a CDW gap. A very rough estimate of the size of the gap yields value of about 320 meV, as indicated by the dashed lines in Figure 4.20. As described in Section 2.2.2, the measurements of local density of states at room tem-

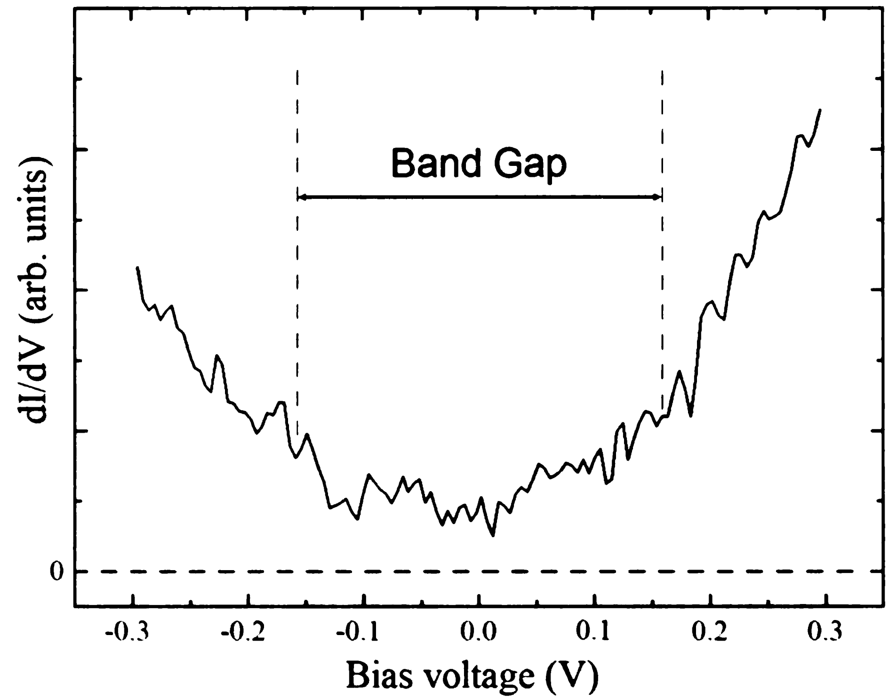

Figure 4.20: Local DOS around Fermi level for YTe_3. dI/dV curve was obtained from I vs. V data measured by sweeping the bias voltage in range ± 300mV. The data is very noisy, but it gives hints on the size of CDW gap. Dashed vertical lines are guides for the eyes. Our estimate for the CDW gap size in YTe_3 is about 320 meV.

perature are smeared out, an effect estimated to be approximately 90 meV, which represents an additional uncertainty of the gap size. To the best of our knowledge, one other measurement of the CDW gap size of YTe_3 has recently been performed by Brouet and collaborators using ARPES, that gave the gap size of 335 meV [120].

4.8 Summary

STM and STS measurements of the $CeTe_3$ at room temperature and 77 K and YTe_3 at room temperature were performed. The one-dimensional CDWs are observed on the surfaces of $CeTe_3$ and YTe_3. In the Fourier transform analysis of the STM images of $CeTe_3$, we observed a peak at $q_{CDW} \approx 2/7 \times 2\pi/c$, as well as several additional peaks. We explored several possible interpretations concerning these peaks, in an attempt to characterize the nature of the CDW in $CeTe_3$. Our FT analysis cannot unambiguously differentiate between the discommensurated and uniformly incommensurate CDW. The principal reason for this is lack of a reliable criterion that would allow us to distinguish whether these extra peaks are satellite peaks to the CDW peak, which would suggest the discommensurated nature of the CDW, or the peaks originate from the artifacts of STM measurement. In the interpretation that supports discommensurated picture we obtained the commensurate domain size that agrees reasonably well with the estimate made by the atomic PDF study [96]. However, we believe the extra peaks in our FT data can be better explained within a wave vector mixing picture, that does not invoke discommensurations.

There are two possibilities for reconciliation of PDF and STM observations. As I have shown, subsurface effects affect STM signal which gives extra peaks in FT. First, the intensity of the satellite peaks is possibly weak compared to these extra peaks. A hint that this could be a case is found in the case of FT of 77 K data (Figure 4.14, small peak at position $\sim 5.5\ \mathrm{nm}^{-1}$). Second, the domain size obtained from the PDF study is possibly underestimated. Larger domain size would result in satellite peaks closer to the fundamental peaks in FT, and would not be resolved in our STM data.

We also measured the local density of states using the STS mode at 77 K, and obtained the CDW gap at various places on the surface of the sample. The gap size obtained in measurements directly above the Te atoms is $\sim$ 360 meV, in good agreement with the ARPES result [95]. The data obtained from measurements on YTe_3 were not of sufficient quality to perform the FT analysis. The CDW gap in YTe_3 obtained from room temperature STS was estimated to be roughly 320 meV.

Chapter 5

Characterizing electronic structure of β-$K_2Bi_8Se_{13}$ thermoelectric using STS

5.1 Introduction

One of the technologically important and scientifically challenging subjects of contemporary condensed matter physics is the field of thermoelectricity. Thermoelectricity is a phenomenon that involves induction of electric potential across a system whose ends are exposed to a temperature gradient, and conversely, generation of a temperature gradient in a sample across to which an electric voltage is applied [121, 18, 122, 123]. Good thermoelectric materials should have their thermal conductivity minimized, and at the same time should have their electric carrier transport maximized [19], as discussed below. It has been a challenge in the past few decades to search for and engineer new thermoelectric materials suitable for commercial applications. In the mid 1950's it was recognized that semiconductors can be superior thermoelectric materials over metals [124, 122]. This comes about due to the fact that in metals the ratio of thermal to electrical conductivity is proportional to temperature (Wiedemann-Franz law). In contrast, semiconductors can have a higher ratio of electrical to thermal conductivity, and can also be doped to allow for this ratio to be tuned to optimize thermoelectricity. More recently, it has also been recognized that structural disorder plays an important role in promising bulk thermoelectric materials. An important part of the process of optimization is proper characterization of the properties of these materials, including the assessment of precise information regarding their electronic structure. Here I present results of STS characterization of one such promising material, $K_2Bi_8Se_{13}$.

5.2 Fundamentals of thermoelectrics

5.2.1 Historic highlights

Thermoelectricity has its foundations in three mutually related phenomena, namely the Seebeck, Peltier, and Thomson effects. Thomas Johann Seebeck in 1821 first discovered the thermoelectric phenomenon, when he noticed that a temperature gradient placed across a metal sample caused a potential difference (thermoelectric electomotive force) across the sample. If two opposite ends of such a sample are placed in contact with high and low temperature surfaces respectively, then the charge carriers in the conductor move in the direction from the hot end towards the cold end. This current will flow until a voltage builds up at the metal ends to cancel the thermoelectric voltage. The same effect is observed in a closed loop, called a thermocouple, formed of two metals or semiconductors, if their junctions are exposed to different temperatures. This effect is described mathematically as

$$E = \frac{dV}{dr} = S\frac{dT}{dr} = S\nabla T, \tag{5.1}$$

where T is temperature, V is the thermoelectric voltage, E is the resultant electric field, which is proportional to the temperature gradient along direction r, and S is the Seebeck coefficient or the thermopower. The thermopower is characteristic of a material, and depends on the material's average temperature, and crystal structure.

The Peltier effect, which is the reverse of the Seebeck effect, was observed by Jean Peltier in 1834. It represents generation of heat difference as a result of applied voltage difference across the sample (typically a junction of two different materials, metals or semiconductors), and is often used for thermoelectric cooling. Essentially, as the electric current runs through a sample, heat flows from one part of the sample to another. In one such setup, when current passes through a circuit of two different conductors, a thermal effect is found at the junctions. The temperature at the junction would increase or decrease depending on the direction of the current flow. The rate of heat flow dQ/dt is then proportional to the magnitude of the current I through the sample,

$$\frac{dQ}{dt} = \Pi I, \tag{5.2}$$

where Π represents the Peltier coefficient that determines how much heat is carried per unit charge through a material. More insight into these phenomena was brought by work of William Thomson in 1854, who determined the thermodynamic relationships behind the effects. This work described the coupling between thermal and electrical currents:

$$J = \sigma \left[E - S \nabla T \right], \tag{5.3}$$

and

$$Q = (\sigma T S) E - \kappa \nabla T, \tag{5.4}$$

where J is the electrical current density, σ is the electrical conductivity, Q is the heat current density, and κ is the thermal conductivity. It has been shown that the Peltier coefficient and the thermopower are related through $\Pi = ST$, which is known as the Kelvin relation. Thermoelectric materials are often discussed in terms of their thermopower rather than their Peltier coefficient simply because S is easier to obtain from experiments [125].

Both electron and hole transport determine the net thermopower in a material, such that:

$$S_{net} = \frac{\sigma_e S_e + \sigma_h S_h}{\sigma_e + \sigma_h}, \tag{5.5}$$

where S_e and σ_e, and S_h and σ_h are the thermopower and electrical conductivity of the electrons and holes respectively. Because metals have partially-filled bands, they typically have small thermopowers. At finite temperature some electrons are thermally excited above the Fermi energy, leaving the holes below the Fermi energy. Since electrons and holes contribute in opposite ways (S_e is negative, whereas S_h is positive), they cancel each other's contribution and make S_{net} small. In contrast, semiconductors can be doped with an excess amount of electrons (n-type) or holes (p-type). Therefore, semiconductors can have large positive or negative values of S_{net} depending on the charge of the excess carriers. In order to determine which charged carriers dominate the electric transport in both metals and semiconductors, one can determine the sign of S_{net} in an experiment. Semiconductors with energy gaps of the order of $10\mathrm{k}_B\mathrm{T}_{max}$, where k_B is the Boltzman constant, and T_{max} is the maximum operating temperature represent good candidates as thermoelectric materials [125] suitable for thermoelectric devices to be used for cooling or generation of electricity directly from a heat source.

5.2.2 Thermoelectric figure of merit and good thermoelectric materials

Good thermoelectric materials require a combination of electrical and thermal properties. The dimensionless figure of merit ZT provides a measure of efficiency of a thermoelectric material as a function of temperature:

$$ZT = \frac{\sigma S^2 T}{\kappa_L + \kappa_e}, \tag{5.6}$$

where κ_L and κ_e represent lattice and electron contributions to the net thermal conductivity. A material is characterized as a better thermoelectric if ZT has a higher value. In order to achieve high ZT, the material must simultaneously possesses high σ, high S, and low κ. Manipulating the thermal conductivity of a material is one of the essential parameters in optimizing properties of new promising bulk materials for thermoelectric applications [19]. In particular, the lattice component, which is the phonon thermal conductivity, can be reduced appreciably by increased phonon scattering in systems with considerable structural disorder. Present efforts in developing high-performance thermoelectric materials are focused on engineering various superlattices and nanowire systems, some of which utilize nonequilibrium effects to decouple electron and phonon transport, to increase S and reduce κ [122].

As the key to the commercial applicability is high efficiency of a thermoelectric material reflected in a high ZT [19], a large body of work is focused on searching for materials with enhanced thermoelectric properties.

Material classes that are intensively studied at present as prospective thermoelectrics, where thermal conductivity can be appreciably reduced, include chalcogenides [126, 127, 128] with complex structures, metal oxides [129, 130, 131], or skutterudites [132, 133, 134] that incorporate large "rattler" atoms in their cage-like structures, acting as phonon-scattering centers. β-$K_2Bi_8Se_{13}$ studied in this work belongs to the class of complex chalcogenides, containing "rattlers", and is promising for thermoelectric applications due to highly anisotropic structure with low symmetry, having low thermal conductivity.

Three parameters relevant for optimizing ZT, σ, S and κ_e, are determined by the details of the electronic properties including the size and structure of the semiconduc-

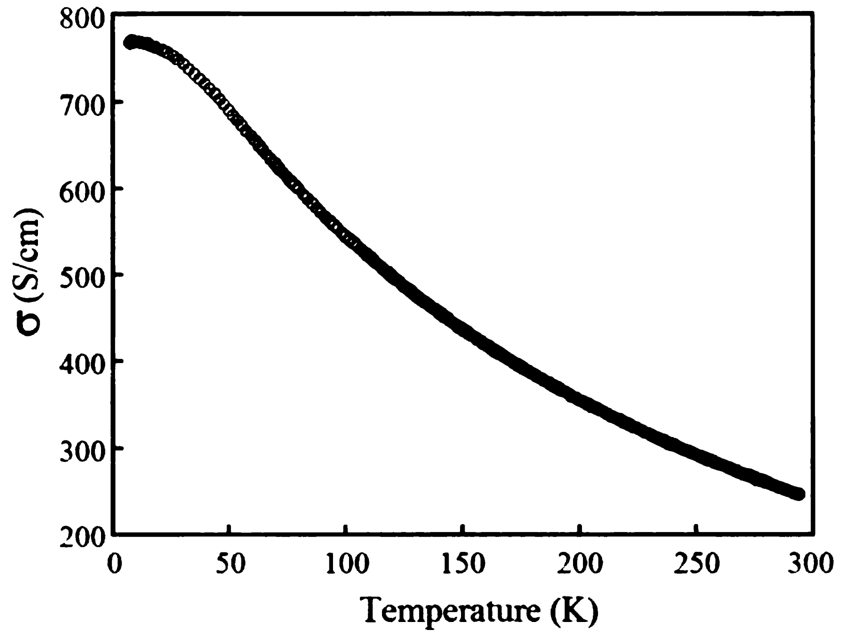

Figure 5.1: Electrical conductivity of single crystal β-$K_2Bi_8Se_{13}$ sample [20].

tor band gap and scattering of charge carriers by defects and impurities. Therefore, understanding the electronic structure of thermoelectric materials is key to optimizing their thermoelectric properties. Scanning tunneling spectroscopy is a powerful tool capable of providing important information on the electronic structure of materials.

5.3 $K_2Bi_8Se_{13}$

5.3.1 Properties

One of the promising candidates for room temperature thermoelectrics is the complex chalcogenide $K_2Bi_8Se_{13}$ [20], which crystalizes in two distinct phases, α-$K_2Bi_8Se_{13}$ and β-$K_2Bi_8Se_{13}$. The α-phase contains no structural disorder, it is a wide band-gap ($\sim$ 0.76 eV) semiconductor, and is not a good thermoelectric, as it has rather low electrical conductivity of 2 S/cm at room temperature. On the other hand, the β-phase is structurally disordered [135, 136], it is a narrow band-gap semiconductor and shows great promise for room temperature thermoelectric. Its room temperature

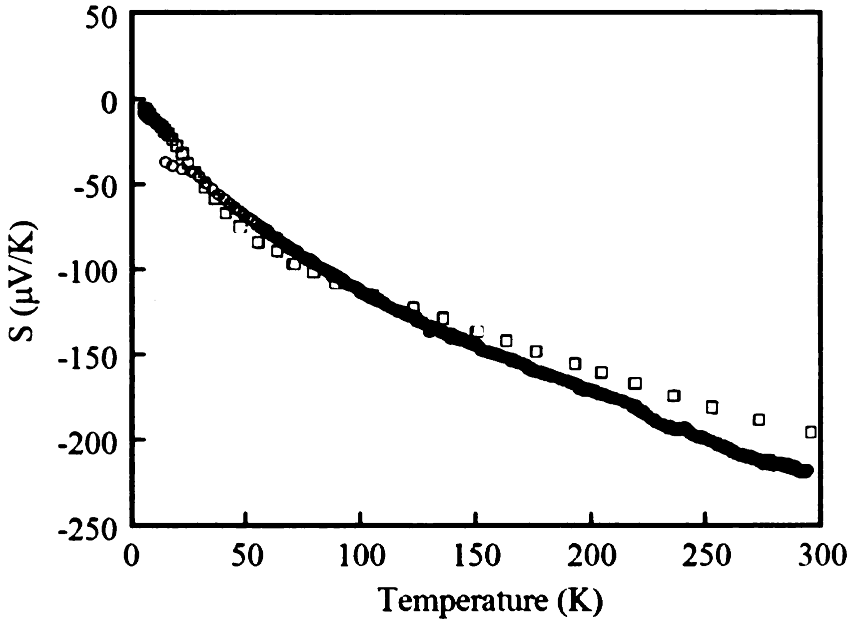

Figure 5.2: Seebeck coefficient of β-$K_2Bi_8Se_{13}$ for single crystal (open circles) and powder (open squares) samples [20].

electrical conductivity is about 250 S/cm (Figure 5.1), it has a Seebeck coefficient of -200 μV/K (same as in the α-phase) (Figure 5.2), and thermal conductivity of 1.28 W/m·K [20]. The negative sign of the Seebeck coefficient indicates that the charge carriers are electrons. The corresponding unitless thermoelectric figure of merit, ZT, is shown in Figure 5.3. The β-phase has a crystal and electronic structure that can lead to a high Seebeck coefficient. It also has a low thermal conductivity that arises from a large, low-symmetry unit cell and weakly bonded K^+ ions, occupying space in tunnels present in the structure that act as "rattlers" [137] and hence phonon-scattering centers. The thermopower is given by the Mott formula

$$S = \frac{\pi^2}{3}\frac{k_B^2 T}{e}\frac{d\, ln\sigma(E)}{dE}, \quad E = E_F \tag{5.7}$$

where σ(E) is the electrical conductivity, whose logarithmic derivative with respect to energy is taken at Fermi energy E_F [138, 139]. If the scattering of charge carriers is independent of their energy E, then σ(E) is proportional to the density of states

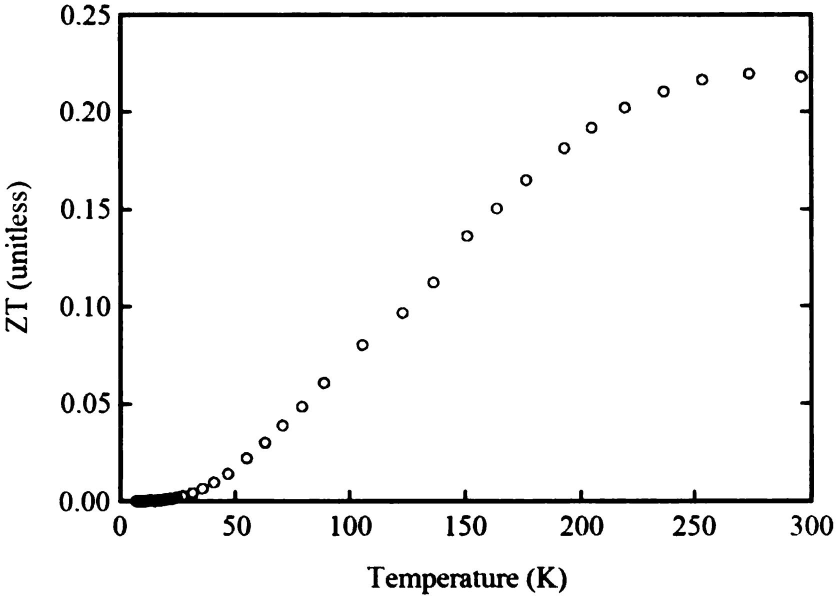

Figure 5.3: ZT of single crystal β-$K_2Bi_8Se_{13}$ sample [20].

at E [20], and the carrier velocity. As the thermopower S depends on the change of σ(E) across the Fermi surface via the logarithmic derivative, manipulation of the density of states near the Fermi level will affect the energy dependence of σ(E); hence both electrical conductivity and thermopower can be changed.

5.3.2 Crystal and electronic structure of β-$K_2Bi_8Se_{13}$

β-$K_2Bi_8Se_{13}$ has a complex low-symmetry structure described within a monoclinic space group with 46 atoms in the unit cell. The lattice parameters are a=17.492Å, b=18.461Å, c=4.205Å, and γ=90.49°. Its highly anisotropic structure results in needle-like morphology along the c crystallographic axis. While the structure shown in Figure 5.4 is rather complex, of interest for this work are some specific features, and I am going to focus our attention on these. The structure includes two different interconnected types of Bi/Se building-blocks and K^+ ions in chains between these blocks. The two different Bi/Se blocks are connected to each other at special mixed occupancy K/Bi sites, circled in Figure 5.4 and labeled K1/Bi9 and Bi8/K3. The original crystallographic study [20] found that these sites, forming chains along the c

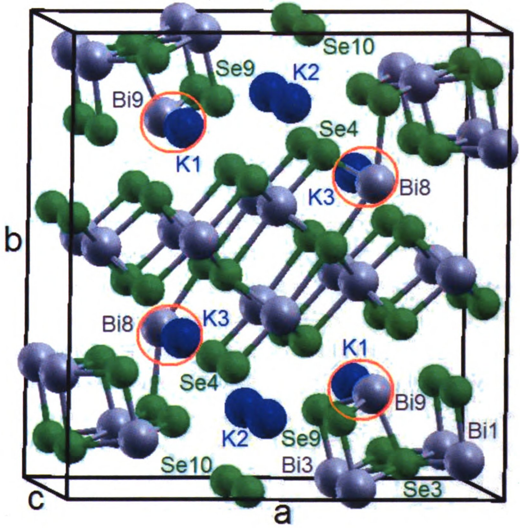

Figure 5.4: (This figure is presented in color.) Crystal structure of β-$K_2Bi_8Se_{13}$ [20]. The structure shown represents the unit cell doubled in the c direction. Large blue spheres represent K atoms, large gray spheres denote Bi atoms, while small green spheres show Se atoms. K/Bi sites of interest for this study that form chains in the structure along c direction are circled. See text for details. Figure courtesy of D. Bilc.

direction, have mixed occupancy, K1/Bi9 containing 62% K and 38% Bi, and Bi8/K3 containing 62% Bi and 38% K. Mixing of K and Bi on these crystallographic sites appears to be crucial in defining the electronic structure near the Fermi level, and consequently governing the electronic properties [20]. This is further supported by the results of *ab-initio* electronic band structure calculations on this compound [135]. These calculations are based on density functional theory, using the same methods introduced in Section 4.5.1. These calculations indicated that the mixed occupancy is crucial for the system to be semiconducting, because Bi atoms at the mixed sites stabilize the $4p$ orbitals of nearest-neighbor Se atoms by lowering their energy, hence allowing the band gap to form.

In order to understand the role that chemical disorder plays in the electronic structure, three different models were considered by D. Bilc and coworkers [135]: two corresponding to chemically homogeneous chains, and one that involves heterogeneous chains, as further discussed. Two different ordered structures with extreme occupancies of K and Bi atoms at the mixed sites were considered. In configuration I, the Bi8/K3 site was occupied solely by Bi, while the K1/Bi9 site contained K only. The other homogeneous configuration, configuration II, was the opposite of configuration I, with a K atom on the Bi8/K3 site, and a Bi atom on the K1/Bi9 site. The system was found to be a semi-metal for both homogeneous structures, in contrast to the experimental fact that the system has semiconducting behavior, with a semiconducting band-gap of 0.56 eV as observed in infrared diffuse reflectance spectra [20]. Therefore, further theoretical considerations had to involve $1\times1\times2$ super-cell containing 92 atoms per cell, in order to accommodate alternative occupancy of K and Bi atoms at the mixed sites (configuration III). As opposed to the case of homogeneous chains, where Se9 and Se4 atoms (see Figure 5.4) had either K or Bi as nearest neighbors, in the model involving chains of alternating K and Bi atoms, Se9 and Se4 atoms had both K and Bi as nearest neighbors. Results of the band structure calcu-

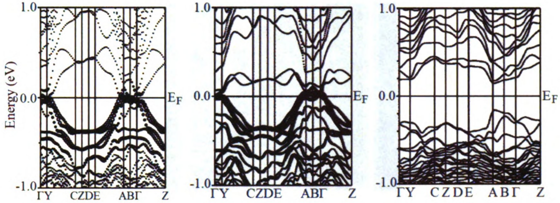

Figure 5.5: Band structure of β-$K_2Bi_8Se_{13}$ as obtained from theoretical considerations for three different configurations of atoms along K/Bi chains. See text for details. Figure adapted from D. Bilc *et al* [135].

lations showed that the system is an indirect band gap semiconductor, with the band gap value of about 0.41 eV. Figure 5.5 summarizes these theoretical findings. From left to right, this figure shows a sequence of calculated electronic band structures of β-$K_2Bi_8Se_{13}$ for configurations I, II, and III, with the band-gap clearly observed in the last case.

Hence, we see that the Bi/K disorder in β-$K_2Bi_8Se_{13}$ has a profound effect on the band structure near the Fermi level, and has been suspected to reduce thermal conductivity [20]. Depending on the position of the atoms in the mixed sites, either narrow band gap semiconducting or semi-metallic behavior is found [135]. The calculated band gap, however, is smaller than the measured value of 0.56 eV.

In order to clarify the reasons behind the mismatch between the theoretical and experimental band gap value, as well as to understand the electronic band structure of this material in greater detail, I used scanning tunneling spectroscopy to assess the electronic structure of β-$K_2Bi_8Se_{13}$ at low temperature. This provides an important experimental reference allowing for more substantial theoretical considerations to take place, aimed to differentiate various types of disorder and their role in electronic structure.

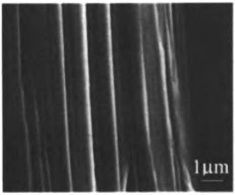

Figure 5.6: SEM image of needle-like structure of β-$K_2Bi_8Se_{13}$. Figure courtesy of T. Kyratsi.

5.4 Scanning tunneling spectroscopy of β-$K_2Bi_8Se_{13}$

5.4.1 Sample synthesis

β-$K_2Bi_8Se_{13}$ sample used in this study was prepared by T. Kyratsi and was obtained by reacting stoichiometric combination of elemental K, Bi, Se as follows. All manipulations were carried out under a dry nitrogen atmosphere in a Vacuum Atmospheres Dri-Lab glove-box. A mixture of 0.282 g of K, 6.021 g of elemental Bi, and 3.697 g of elemental Se was loaded into silica tube, which was subsequently flame-sealed at a residual pressure of $<10^{-4}$ Torr. The mixture was heated to 850 °C over 12 hours and kept there for 1 hour, followed by slowly cooling to 450 °C and kept there for 48 hours, and cooling to 50 °C at a rate of -15 °C/h. The product was annealed at 450 °C for 48 hours to ensure phase purity of β-$K_2Bi_8Se_{13}$. Metallic black needles of β-$K_2Bi_8Se_{13}$ were obtained by isolation in dimethylformamide and washing with diethyl ether. A quantitative microprobe analysis with electron microprobe energy dispersive spectroscopy (EDS) was performed on several crystals of the compound to verify the stoichiometry. Scanning electron microscope (SEM) images of the sample confirms a highly oriented needle-like morphology of β-$K_2Bi_8Se_{13}$, as shown in Figure 5.6.

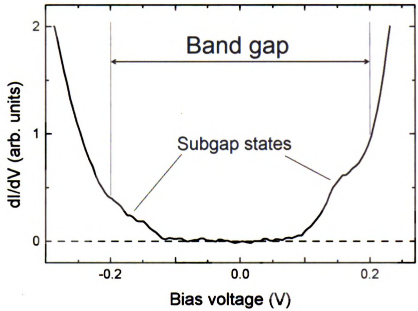

Figure 5.7: Local density of states of β-$K_2Bi_8Se_{13}$ as obtained by the STS measurements at 1.6 K. From the data, a band-gap of ~ 0.4 eV is estimated, in agreement with theoretical prediction [135] based on configuration III that assumes alternating K/Bi chains. In addition, subgap states are observed. See text for details.

5.4.2 Results and discussion

Using the STM point spectroscopy mode, the energy band gap at the sample surface was probed and its size was estimated. The STS measurements on a cleaved surface of β-$K_2Bi_8Se_{13}$ were performed at 1.6 K temperature for various positions of the probing tip above the surface of the sample. Sweeping the bias voltage V over a range of ± 300 mV, I have measured tunneling current I as a function of the ramped voltage. Differentiation of $I(V)$ data with respect to V gives the local density of states, as has been explained in the STM spectroscopy Section 2.2.2. The measurements for a given tip position were repeated 100 times, and averaged, in order to improve signal to noise ratio.

Measured local density of states of β-$K_2Bi_8Se_{13}$ at 1.6 K temperature is shown in Figure 5.7. The data clearly indicate the presence of the band gap. The magnitude of the observed gap of ~ 0.4 eV agrees reasonably well with the calculated value based on configuration III described earlier, that assumes chains with alternating K/Bi atoms [135]. The discrepancy between our STS result for the band gap size, and that of ~ 0.56 eV obtained from optical measurements [20] can be understood if the band gap in β-$K_2Bi_8Se_{13}$ is indeed indirect [135], as the bottom of the conduction band and the top of the valence band would be offset along the momentum axis. The key difference between the optical and tunneling measurements of the band gap is that optical measurements are sensitive to wave vector $\mathbf{k}$, while tunneling measurements are not. Hence optical measurements can get larger gap values. According to theoretical calculations by Bilc *et al.* [135] the band gap in β-$K_2Bi_8Se_{13}$ is almost direct, in which case results of tunneling and optical measurements should approximately agree.

We should note that the surface of the sample exhibited relatively rough texture and was not easily cleavable. Due to the surface roughness and as a result of the coarse approach of the sample with slight sideways motion, the tip became blunt on the atomic scale, and the atomic STM resolution necessary to obtain real space surface topography was not achieved. Consequently, the density of states obtained in our measurements is not truly local, but rather represents a spatial average over several atomic sites on the sample surface.

As can be seen in Figure 5.7, the STS data indicate the presence of subgap states, seen as an enhancement of the density of states in the gap region near the top of the valence band and bottom of the conduction band. One possible explanation of the origin of these states could be the presence of disorder. More specifically, “less mixed” segments along the chains composed of Bi8/K3 sites and of K1/Bi9 sites may shift the energy states into the gap, making it narrower.

It is indeed plausible that in the real material there exist regions close to configurations I and II, which may create such subgap states, which are not predicted by configuration III. It is of particular importance to verify if this is really the case,

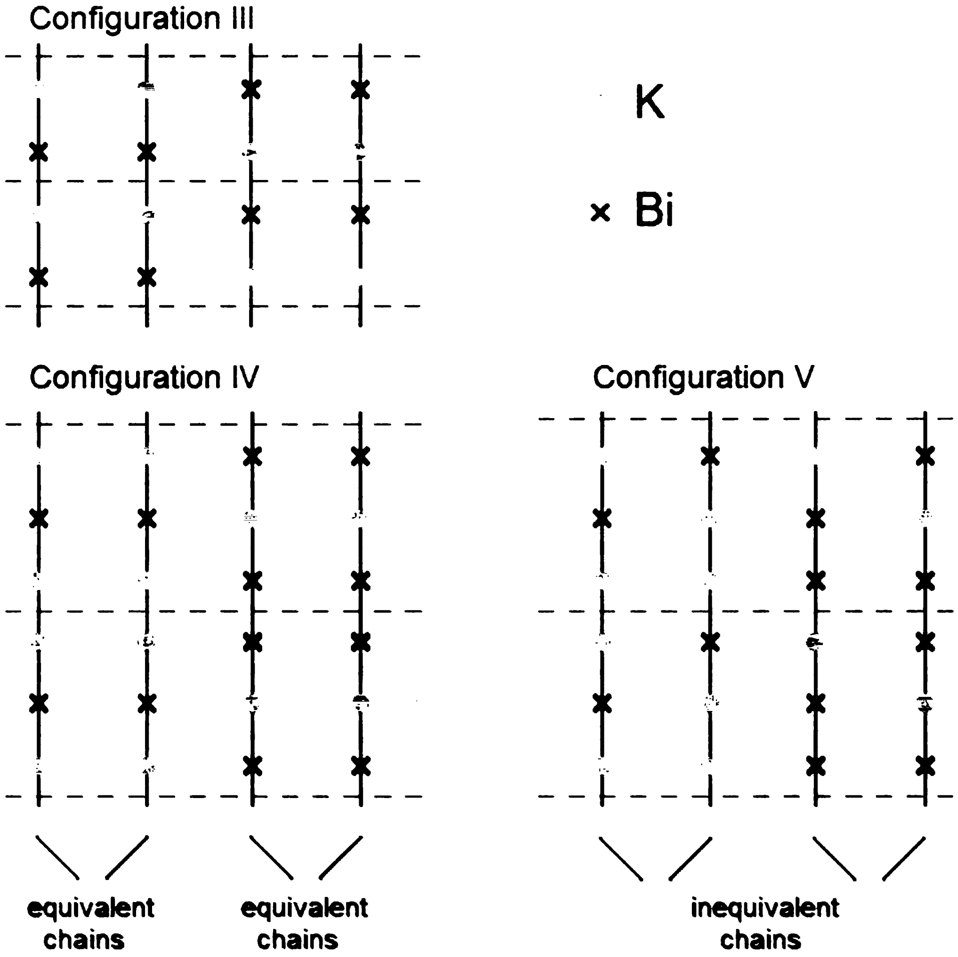

Figure 5.8: Schematic representation of various configurations of the K/Bi chains considered in theoretical calculations. K atoms are represented with solid circles, while Bi atoms are represented with cross-marks. There are four K/Bi chains of interest in the original unit cell, however there are only two inequivalent chain types, K1/Bi9 and Bi8/K3. Configuration III requires unit cell doubling along the chain direction and assumes chains of alternating K and Bi, such that two inequivalent chains have opposite ordering phase. Configuration IV requires unit cell tripling along the chain direction, with K1/Bi9 chain type having K-Bi-K sequence, while Bi8/K3 type features Bi-K-Bi sequence. Configuration V also requires tripling of the unit cell, and is closely related to configuration IV, except that all four chains are now made inequivalent, by offsetting the phase along the equivalent chains.

as these states would change the density of states near the Fermi level, and would contribute to the charge transport, raising the values of electrical conductivity and thermopower [135]. If the nature of the observed subgap states could be characterized through electronic band structure calculations, this would also provide an information of possible structural motifs involved along the disordered K/Bi chains.

In collaboration with group of Dr. Mahanti, and motivated by the observation of the subgap states, further theoretical calculations have been carried out by K. Hoang using various configurations along K/Bi chains. These configurations are shown in Figure 5.8, representing several different variants of K/Bi interchain disorder. We note here that within the unit cell of β-$K_2Bi_8Se_{13}$ there are four K/Bi chains of interest in the original unit cell; however there are only two inequivalent chain types, K1/Bi9 and Bi8/K3. Configuration III requires unit cell doubling along the chain direction and assumes chains of alternating K and Bi, such that two inequivalent chains have opposite ordering phase. Configuration IV assumes interchain disorder and requires unit cell tripling along the chain direction, with K1/Bi9 chain type having K-Bi-K sequence, while Bi8/K3 type features Bi-K-Bi sequence. Configuration V also requires tripling of the unit cell, and is closely related to configuration IV, except that all four chains are now made inequivalent, introducing intrachain disorder between previously equivalent chains by offsetting the phase along the equivalent chains.

The resulting DOS obtained in preliminary electronic band structure calculations are shown in Figure 5.9 for all three configurations considered. Since the theoretical calculations did not include spin-orbit interaction, the size of the theoretical band gaps are overestimated [21]. The results of the calculations allowed for the following observations to be made. On going from configuration III to configuration IV, the band gap size decreases. In addition, Se9 states that occur near the top of the valence band get redistributed towards lower energies, as these states are strongly affected by the structure of neighboring K1/Bi9 chains. Se9 has the K1/Bi9 chain atoms as

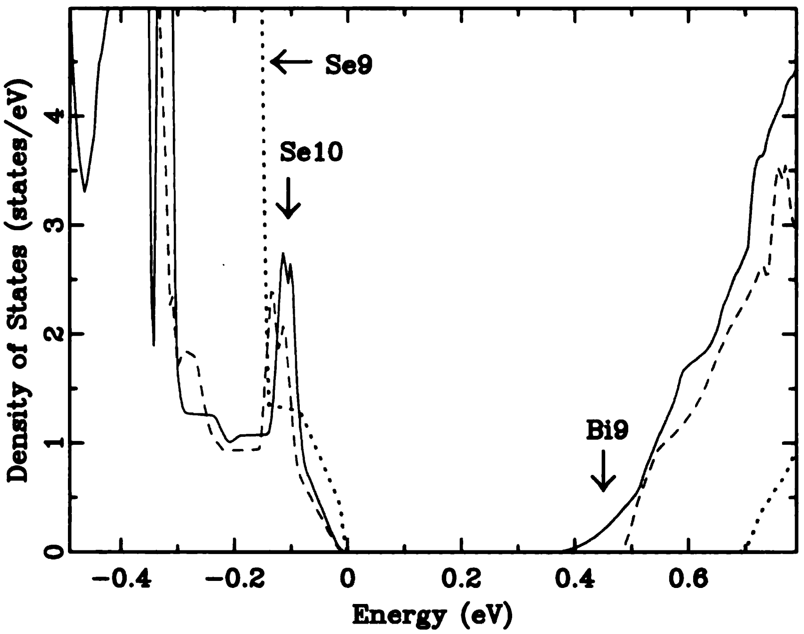

Figure 5.9: DOS obtained from the electronic band structure calculations considering three different configurations along the K/Bi chains: configuration III (dotted line), configuration IV (dashed line), and configuration V (solid line). Arrows indicate specific features discussed in the text.

nearest neighbors. The energy range of our STS measurements was not sufficiently wide to involve region where Se9 states occur.

On the other hand, Se10 states that are also near the top of the valence band do not get affected by the changes in the chains, since Se10 atoms are sufficiently far from the chains. On going from configuration IV to configuration V, the following observations are made. Se10 states near the valence band top do not change, as expected. However, changes occur near the bottom of the conduction band, that may be significant in understanding the subgap states observed by STS. According to the results of electronic band structure calculations for configuration V [140], the bottom of the conduction band is filled with states related to K/Bi chains. In particular, it has been found that these states are predominantly of Bi9 character, and relate to chains where Bi9 atoms are sandwiched between K1 dimers. In other words it is Bi atoms within the disordered chains that give rise to the DOS at the bottom of the

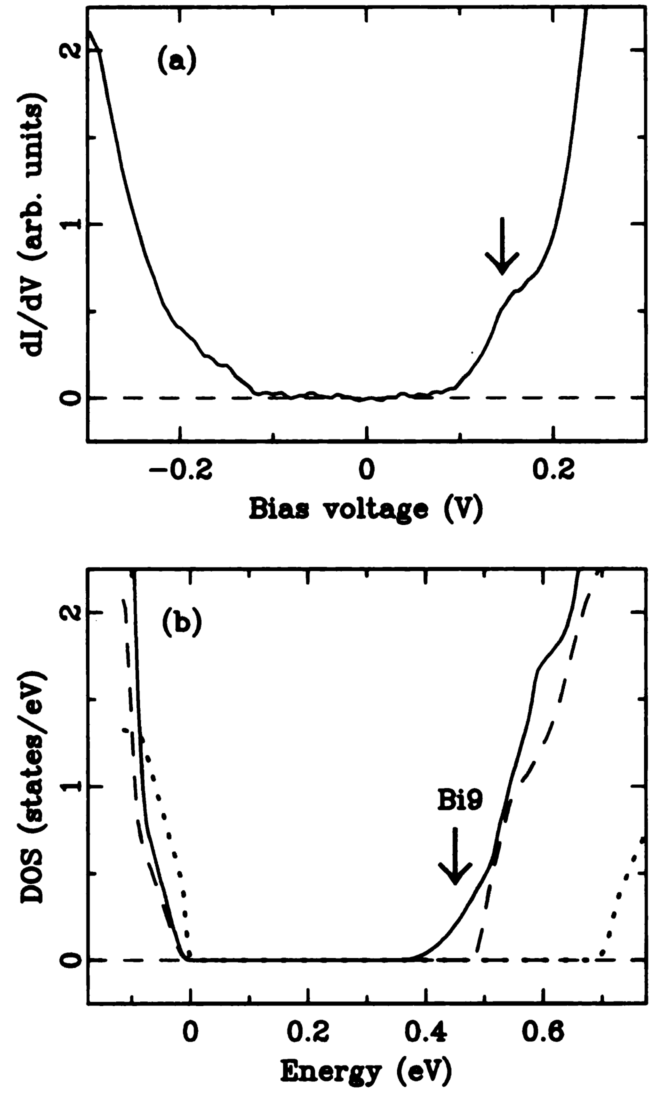

Figure 5.10: (a) STS data for DOS near the Fermi level of β-$K_2Bi_8Se_{13}$, at 1.6 K. (b) DOS obtained from the electronic band structure calculations considering three different configurations along the K/Bi chains: configuration III (dotted line), configuration IV (dashed line), and configuration V (solid line). The arrows in both panels indicate features of interest discussed in text.

conduction band. On the other hand, the contribution to the subgap states from Bi8/K3 chains, where Bi8 dimers are sandwiched between K3 atoms, is not appreciable. A comparison of density of states obtained experimentally and theoretically is shown in Figure 5.10, with notable similarity of the experimental curve and the calculated one for configuration V in the energy range of the measurement.

5.5 Summary

The local electronic structure near the Fermi level of β-$K_2Bi_8Se_{13}$, a promising thermoelectric material, was studied using scanning tunneling spectroscopy. This material is a narrow band gap semiconductor, and the STS experiment at 1.6 K temperature revealed a gap of approximately 0.4 eV, in good agreement with results of theoretical calculations. Further, the STS study revealed the presence of subgap states that, according to recent electronic band structure calculations exploring several K/Bi chain configurations, represent a signature of disorder along K1/Bi9 and Bi8/K3 chains. This disorder significantly influences the electronic structure and narrows the band gap. This further suggests that the subgap states near the bottom of the conduction band are predominantly of Bi9 character. On the other hand, the subgap states near the top of the valence band can be attributed to Se10. The disorder in β-$K_2Bi_8Se_{13}$ could play an important role for its thermoelectric properties, by changing the density of states near the band gap and perhaps increasing the thermopower.

Chapter 6

Concluding remarks

6.1 Summary

Scanning tunneling microscopy and spectroscopy represent important tools providing valuable information about electronic structure of complex materials, allowing for better understanding of their physical properties. In this work we studied the electronic structure of samples belonging to two different classes of complex materials, one exhibiting incommensurate CDW, and another that is a promising high-performance thermoelectric. Both of these studies highlight the importance of knowing the details of the electronic structure near the Fermi level for the respective phenomena.

6.1.1 $CeTe_3$ and YTe_3

The charge density wave (CDW) state is one of the competing ground states in anisotropic, low-dimensional materials. $CeTe_3$ as a cleavable, layered system featuring tellurium layers where a stable one-dimensional incommensurate CDW forms, is a model system for incommensurate CDW studies. Scanning tunneling microscopy is a powerful technique to study surface topography and local electronic structure of complex materials. We applied STM and STS to study the electronic properties of the CDW within Te-layers of $CeTe_3$ and related YTe_3. STM and STS measurements of the $CeTe_3$ at room temperature and 77 K and YTe_3 at room temperature were performed. The one-dimensional CDWs were observed on the surfaces of $CeTe_3$ and YTe_3. In Fourier transform analysis of the STM images of $CeTe_3$, we observed the $q_{CDW} \approx 2/7 \times 2\pi/c$ peak, as well as several additional peaks. We explored several possible interpretations concerning these peaks and their relation to the CDW. Our FT analysis cannot unambiguously differentiate between the discommensurated and uniformly incommensurate CDW. The principal reason for this is lack of reliable criterion that would allow us to distinguish whether these extra peaks are satellite peaks to the CDW peak, which would suggest discommensurated nature of the CDW, or the peaks originate from the artifacts of the STM measurement. In the interpretation that supports the discommensurated picture we obtained the commensurate domain size that agrees reasonably well with the estimate made by the atomic PDF study [96]. However, the extra peaks in our FT data can also be explained within the wave vector mixing picture, that does not invoke discommensurations. The local density of states near the Fermi level has also been obtained using the STS mode at 77 K. We obtained the CDW gap at various places on the surface of the sample. The CDW gap size obtained in measurements directly above the Te atoms was ~ 360 meV, in good agreement with ARPES result [95]. The data obtained from measurements on YTe_3 were not of sufficient quality to perform the FT analysis. The CDW gap in YTe_3 obtained from room temperature STS was estimated to be roughly ~ 320 meV.

6.1.2 β-$K_2Bi_8Se_{13}$

The local electronic structure near the Fermi level of β-$K_2Bi_8Se_{13}$, a promising thermoelectric material, was studied using STS. This material is a narrow band gap semiconductor, and the STS experiment at 1.6 K temperature revealed a gap of approximately 0.4 eV, in good agreement with results of theoretical calculations. Our STS study also revealed the presence of subgap states. According to recent electronic band structure calculations exploring several K/Bi chain configurations, the subgap states represent a signature of disorder along the chains. This disorder significantly influences the electronic structure and narrows the band gap. The experimental results of this work, together with the results of the electronic band structure calculations support the idea of K/Bi disorder being present in the system. The disorder in β-$K_2Bi_8Se_{13}$ could play an important role for its thermoelectric properties.

6.2 Future work

On the CDW side, a natural extension of this work would be to study the details of the electronic structure in a systematic way of a broad class of Rare-Earth tritellurides ($RETe_3$ with RE = La, Ce, Pr, Nd, Sm, Gd, Tb, Dy, Ho, Er, Tm). While all of them exhibit the CDW state with different critical temperatures, very few of these materials have their electronic properties fully characterized. It would be therefore beneficial to assess the sizes of the band gaps across the series, for example, and see how this important parameter varies with different RE. Another possible STM study in this class of materials would involve $HoTe_3$, which exhibits two CDW transitions, one present at room temperature, and another below 110 K [110]. At low temperature two CDWs with mutually perpendicular CDW wave vectors are expected. The experiments aimed in assessing the CDW surface structure as well as spectroscopy would be carried out in both CDW states at room temperature and at 77 K, to investigate the electronic structure in this material.

Another direction for this research follows from the magnetic properties, as it has been demonstrated that $CeTe_3$ is a Kondo lattice material [94]. The Kondo effect arises from the interactions between a magnetic atom and the conduction electrons in an otherwise non-magnetic metal. In this case, the magnetic state is the $4f$ level of the cerium ions. The Kondo temperature is roughly 10 K and the system stays in that state down to 2.8 K. Repeating the topographic measurements at liquid helium temperature (4.2 K) and then acquiring spectra with the tip positioned above Ce atoms, the electronic structure of the Kondo lattice system would be resolved with scanning tunneling spectroscopy. Our cryogenic STM system achieves the resolution expected to be necessary to resolve the Kondo features in the local density of states. Theoretical density of states exhibit the basic predicted spectroscopic features using a model system. By comparing the measurements to theory, the study will explore questions of the Kondo lattice system and the interplay with the charge density wave.

Additional experiments could also be carried out on the thermoelectric material β-$K_2Bi_8Se_{13}$, to further investigate the details of the electronic structure using STS. In the present study, the band gap and the subgap states have been observed. However, the energy range probed was insufficiently broad to assess the part near the top of the valence band where, according to the electronic band structure calculations, Se9 states are observed to rearrange dramatically, which could be used as an important indicator in more reliable distinction between various different types of disorder along K/Bi chains.

Bibliography

[1] M. Vershinin, S. Misra, S. Ono, Y. Abe, Y. Ando, and A. Yazdani, Science **303**, 1995 (2004).

[2] J. C. Loudon, S. Cox, A. J. Williams, J. P. Attfield, P. B. Littlewood, P. A. Midgley, and N. D. Mathur, Phys. Rev. Lett. **94**, 097202 (2005).

[3] D. Bilc, S. D. Mahanti, E. Quarez, K.-F. Hsu, R. Pcionek, and M. G. Kanatzidis, Phys. Rev. Lett. **93**, 146403 (2004).

[4] J. W. Lynn, D. N. Argyriou, Y. Ren, Y. Chen, Y. Mukovskii, and D. Shulyatev, cond-mat , 0701001 (2007).

[5] H. J. Kim, E. S. Božin, S. M. Haile, G. J. Snyder, and S. J. L. Billinge, Phys. Rev. B **75**, 134103 (2007).

[6] H. Lin, E. S. Božin, S. J. L. Billinge, E. Quarez, and M. G. Kanatzidis, Phys. Rev. B **72**, 174113 (2005).

[7] E. S. Božin, S. J. L. Billinge, H. Takagi, and G. H. Kwei, Phys. Rev. Lett. **84**, 5856 (2000).

[8] X. Qiu, S. J. L. Billinge, C. R. Kmety, and J. F. Mitchell, J. Phys. Chem. Solids **65**, 1423 (2004).

[9] S. Cox, J. Singleton, R. D. McDonald, A. Migliori, and P. Littlewood, cond-mat , 07054310 (2007).

[10] G. C. Milward, M. J. Calderon, and P. B. Littlewood, Nature **433**, 607 (2005).

[11] A. Mourachkine, Supercond. Sci. Technol. **13**, 1378 (2000).

[12] J. M. Tranquada, B. J. Sternlieb, J. D. Axe, Y. Nakamura, and S. Uchida, Nature **375**, 561 (1995).

[13] H. A. Mook, P. C. Dai, S. M. Hayden, G. Aeppli, T. G. Perring, and F. Dogan, Nature **395**, 580 (1998).

[14] G. Binnig, H. Rohrer, C. Gerber, and E. Weibel, Appl. Phys. Lett. **40**, 178 (1982).

[15] G. Binnig, H. Rohrer, C. Gerber, and E. Weibel, Phys. Rev. Lett. **49**, 57 (1982).

[16] G. Grüner, *Density waves in solids*, Addison Wesley, Reading, MA, 1994.

[17] R. M. Fleming, Phys. Rev. B **22**, 5606 (1980).

[18] G. S. Nolas, J. Sharp, and H. J. Goldsmid, *Thermoelectrics: basic principles and new materials developments*, Springer-Verlag, 2001.

[19] G. S. Nolas, J. Poon, and K. G. Kanatzidis, Mater. Res. Soc. Bull. **31**, 199 (2006).

[20] D. Y. Chung, K. S. Choi, L. Iordanidis, J. L. Schindler, P. W. Brazis, C. R. Kannewurf, B. Chen, S. Hu, C. Uher, and M. G. Kanatzidis, Chem. Mater. **9**, 3060 (1997).

[21] D. Bilc, *Electronic structure and thermoelectric properties of narrow band gap chalcogenides*, Ph.D. Thesis, Michigan State University, 2005.

[22] J. A. Stroscio and W. J. Kaiser, *Scanning Tunneling Microscopy*, Academic Press, Boston, 1993.

[23] M. Tinkham, *Introduction to superconductivity*, Robert. E. Krieger Publishing Company, Malabar, Florida, 1980.

[24] E. Stoll, A. Baratoff, A. Selloni, and P. Carnevali, J. Phys. C: Solid State Phys. **17**, 3073 (1982).

[25] K. Besocke, Surface Sci. **181**, 145 (1987).

[26] D. Tománek, S. G. Louie, H. J. Mamin, and D. W. Abraham, Phys. Rev. B **35**, 7790 (1987).

[27] J. M. Carpinelli, H. H. Weitering, E. W. Plummer, and R. Stumpf, Nature **381**, 398 (1996).

[28] J. A. Wilson, F. J. DiSalvo, and S. Mahajan, Phys. Rev. Lett. **32**, 882 (1974).

[29] J. M. Tranquada, D. J. Buttrey, V. Sachan, and J. E. Lorenzo, Phys. Rev. Lett. **73**, 1003 (1994).

[30] V. Sachan, D. J. Buttrey, J. M. Tranquada, J. E. Lorenzo, and G. Shirane, Phys. Rev. B **51**, 12742 (1995).

[31] S. Mori, C. H. Chen, and S.-W. Cheong, Nature **392**, 473 (1998).

[32] T. Hanaguri, C. Lupien, Y. Kohsaka, D.-H. Lee, M. Azuma, M. Takano, H. Takagi, and J. C. Davis, Nature **430**, 1001 (2004).

[33] S. Komiya, H.-D. Chen, S.-C. Zhang, and Y. Ando, Phys. Rev. Lett. **94**, 207004 (2005).

[34] M. I. Salkola, V. J. Emery, and S. A. Kivelson, Phys. Rev. Lett. **77**, 155 (1996).

[35] R. E. Thorne, Physics Today **5**, 42 (1996).

[36] S. Brown and G. Grüner, Scientific American **4**, 50 (1994).

[37] R. E. Peierls, *Quantum theory of solids*, Clarendon Press, Oxford, 1955.

[38] H. Akamatu, H. Inokuchi, and Y. Matsunaga, Nature **173**, 168 (1954).

[39] L. B. Coleman, J. A. Cohen, A. F. Garito, and A. J. Heeger, Phys. Rev. B **7**, 2122 (1973).

[40] P. W. Anderson, P. A. Lee, and M. Saitoh, Solid State Commun. **13**, 595 (1973).

[41] M. J. Rice and S. Strässler, Solid State Commun. **13**, 1389 (1973).

[42] S. van Smaalen, Acta Crystallogr. A **61**, 51 (2005).

[43] A. Damascelli, Physica Scripta **T109**, 61 (2004).

[44] M. A. Valbuena, J. Avila, S. Drouard, H. Guyot, and M. C. Asensio, J. Phys. Chem. Solids **67**, 213 (2006).

[45] C. J. Chen, *Introduction to Scanning Tunneling Microscopy*, Oxford Science Publications, Oxford, 1993.

[46] N. Magonov and M.-H. Whangbo, *Surface analysis with STM and AFM*, VCH Publishers, Weinheim, 1996.

[47] P. Mallet, K. M. Zimmermann, P. Chevalier, J. Marcus, J. Y. Veuillen, and J. M. G. Rodriguez, Phys. Rev. B **60**, 2122 (1999).

[48] N. P. Ong and P. Monceau, Phys. Rev. B **16**, 3443 (1977).

[49] B. E. Warren, *X-ray diffraction*, Dover, New York, 1990.

[50] G. E. Bacon, *Neutron diffraction*, Oxford University Press, Oxford, 1975.

[51] B. Fultz and J. M. Howe, *Transmission Electron Microscopy and Diffractometry of Materials*, Springer-Verlag, Berlin, 2002.

[52] P. Foury and J. P. Pouget, Int. J. Mod. Phys. B **7**, 3973 (1993).

[53] D. D. Laws, H. L. Bitter, and A. Jerschow, Angew. Chem. Int. Edit. **41**, 3096 (2002).

[54] J. H. Ross, Z. Wang, and C. P. Slichter, Phys. Rev. B **41**, 2722 (1990).

[55] D. J. Gardiner, *Practical Raman spectroscopy*, Springer-Verlag, Berlin, 1989.

[56] T. Hirata and F. S. Ohuchi, Solid State Commun. **117**, 361 (2001).

[57] G. Grüner, Rev. Mod. Phys. **60**, 1129 (1988).

[58] A. H. C. Neto and C. M. Smith, *Charge Inhomogeneities in Strongly Correlated Systems, in "Strong Interactions in Low Dimensions", D. Baeriswyl and L. Degiorgi Edts.*, Kluwer, Dordrecht, The Netherlands, 2004.

[59] A. M. Gabovich, A. I. Voitenko, and M. Ausloos, Phys. Rep. **367**, 583 (2002).

[60] H. H. Weitering, J. M. Carpinelli, A. V. Melechko, J. Zhang, M. Bartkowiak, and E. W. Plummer, Science **285**, 2107 (1999).

[61] T. Valla, A. V. Fedorov, P. D. Johnson, P. A. Glans, C. McGuinness, K. E. Smith, E. Y. Andrei, and H. Berger, Phys. Rev. Lett. **92**, 86401 (2004).

[62] A. H. C. Neto, Phys. Rev. Lett. **86**, 4382 (2001).

[63] R. J. Cava, P. Littlewood, R. M. Fleming, R. G. Dunn, and E. A. Rietman, Phys. Rev. B **33**, 2439 (1986).

[64] W. G. Lyons and J. R. Tucker, Phys. Rev. B **38**, 4303 (1988).

[65] A. Terrasi, M. Marsi, H. Berger, G. Margaritondo, R. J. Kelley, and M. Onellion, Phys. Rev. B **52**, 5592 (1995).

[66] J. Voit, L. Perfetti, F. Zwick, H. Berger, G. Margaritondo, G. Grüner, H. Höchst, and M. Grioni, Science **290**, 501 (2000).

[67] N. Shannon and R. Joynt, Solid State Commun. **115**, 411 (2000).

[68] S. Sridhar, D. Reagor, and G. Grüner, Phys. Rev. Lett. **55**, 1196 (1985).

[69] S. van Smaalen, J. L. de Boer, A. Meetsma, H. Graafsma, H.-S. Sheu, A. Darovskikh, P. Coppens, and F. Levy, Phys. Rev. B **45**, 3103 (1992).

[70] J. Schäfer, E. Rotenberg, S. D. Kevan, P. Blaha, R. Claessen, and R. E. Thorne, Phys. Rev. Lett. **87**, 196403 (2001).

[71] Y. S. Hor, Z. L. Xiao, U. Welp, Y. Ito, J. F. Mitchell, R. E. Cook, W. K. Kwok, and G. W. Crabtree, Nano Lett. **5**, 397 (2005).

[72] T. Haga, Y. Abe, and Y. Okwamoto, Phys. Rev. Lett. **51**, 678 (1983).

[73] X. L. Wu and C. M. Lieber, Science **243**, 1703 (1989).

[74] R. V. Coleman, V. V. McNairy, and C. G. Slough, Phys. Rev. B **45**, 1428 (1992).

[75] T. Pillo, J. Hayoz, H. Berger, M. Grioni, L. Schlapbach, and P. Aebi, Phys. Rev. Lett. **83**, 3494 (1999).

[76] Y. Toda, K. Tateishi, and S. Tanda, Phys. Rev. B **70**, 33106 (2004).

[77] L. Perfetti, T. A. Gloor, F. Mila, H. Berger, and M. Grioni, Phys. Rev. B **71**, 153101 (2005).

[78] D. E. Moncton, J. D. Axe, and F. J. DiSalva, Phys. Rev. Lett. **34**, 734 (1975).

[79] K. Horiba, K. Ono, J. H. Oh, T. Kihara, S. Nakazono, M. Oshima, O. Shiino, H. W. Yeom, A. Kakizaki, and Y. Aiura, Phys. Rev. B **66**, 073106 (2002).

[80] T. Valla, A. V. Fedorov, P. D. Johnson, J. Xue, K. E. Smith, and F. J. DiSalvo, Phys. Rev. Lett. **85**, 4759 (2000).

[81] M. Bovet, D. Popović, F. Clerc, C. Koitzsch, U. Probst, E. Bucher, H. Berger, D. Naumović, and P. Aebi, Phys. Rev. B **69**, 125117 (2004).

[82] B. Giambattista, C. G. Slough, V. V. McNairy, and R. V. Coleman, Phys. Rev. B **41**, 10082 (1990).

[83] S. C. Bayliss, A. M. Ghorayeb, and D. R. P. Guy, J. Phys. Chem. **17**, L533 (1984).

[84] B. Burk and A. Zettl, Phys. Rev. B **46**, 9817 (1992).

[85] M. Arita, H. Negishi, K. Shimada, F. Xu, A. Ino, Y. Takeda, K. Yamazaki, A. Kimura, S. Qiao, S. Negishi, M. Sasaki, H. Namatame, and M. Taniguchi, Physica B **351**, 265 (2004).

[86] J. A. Wilson, F. J. DiSalvo, and S. Mahajan, Adv. Phys. **24**, 117 (1975).

[87] C. B. Scruby, P. M. Williams, and G. S. Parry, Philos. Mag. **31**, 255 (1975).

[88] A. Yamamonto, Phys. Rev. B **27**, 7823 (1983).

[89] E. DiMasi, M. C. Aronson, J. F. Mansfield, B. Foran, and S. Lee, Phys. Rev. B **52**, 14516 (1995).

[90] R. Patschke and M. G. Kanatzidis, Phys. Chem. Chem. Phys. **4**, 3266 (2002).

[91] C. Malliakas, S. J. L. Billinge, H.-J. Kim, and M. G. Kanatzidis, J. Am. Chem. Soc. **127**, 6510 (2005).

[92] W. Tremel and R. Hoffmann, J. Am. Chem. Soc. **109**, 124 (1987).

[93] E. DiMasi, B. Foran, M. C. Aronson, and S. Lee, Chem. Mater. **6**, 1867 (1995).

[94] N. Ru and I. R. Fisher, Phys. Rev. B **73**, 033101 (2006).

[95] V. Brouet, W. L. Yang, X. J. Zhou, Z. Hussain, N. Ru, K. Y. Shin, I. R. Fisher, and Z. X. Shen, Phys. Rev. Lett. **93**, 126405 (2004).

[96] H. J. Kim, C. D. Malliakas, A. Tomic, S. H. Tessmer, M. G. Kanatzidis, and S. J. L. Billinge, Phys. Rev. Lett. **96**, 226401 (2006).

[97] A. Fang, N. Ru, I. R. Fisher, and A. Kapitulnik, Phys. Rev. Lett. **99**, 046401 (2007).

[98] H. Bestgen, Solid State Commun. **58**, 197 (1986).

[99] A. B. McLean, R. M. Feenstra, A. Taleb-Ibrahimi, and R. Ludeke, Phys. Rev. B **39**, 12925 (1989).

[100] R. Clarke, J. N. Gray, H. Homma, and M. J. Winokur, Phys. Rev. Lett. **47**, 1407 (1981).

[101] C. H. Chen, J. M. Gibson, and R. M. Fleming, Phys. Rev. Lett. **47**, 723 (1981).

[102] W. Lin, H. Steinfink, and E. J. Weiss, Inorg. Chem. **4**, 877 (1965).

[103] B. K. Norling and H. Steinfink, Inorg. Chem. **5**, 1488 (1966).

[104] H. Komoda, T. Sato, S. Souma, T. Takahashi, Y. Ito, and K. Suzuki, Phys. Rev. B **70**, 195101 (2004).

[105] A. Kikuchi, J. Phys. Soc. Jpn. **67**, 1308 (1998).

[106] J. Laverock, S. B. Dugdale, Z. Major, M. A. Alam, N. Ru, I. R. Fisher, G. Santi, and E. Bruno, Phys. Rev. B **71**, 085114 (2005).

[107] H. Chudo, C. Michioka, Y. Itoh, and K. Yoshimura, Phys. Rev. B **75**, 045113 (2007).

[108] G.-H. Gweon, J. D. Denlinger, J. A. Clack, J. W. Allen, C. G. Olson, E. DiMasi, M. C. Aronson, B. Foran, and S. Lee, Phys. Rev. Lett. **81**, 886 (1998).

[109] H. Yao, J. A. Robertson, E.-A. Kim, and S. A. Kivelson, Phys. Rev. B **74**, 245126 (2006).

[110] N. Ru, G. Y. Margulis, K. Y. Shin, M. F. Toney, and I. R. Fisher, cond-mat , 0610319 (2006).

[111] www.imagemet.com.

[112] B. Burk, R. E. Thomson, A. Zettl, and J. Clarke, Phys. Rev. Lett. **66**, 3040 (1991).

[113] R. E. Thomson, B. Burk, A. Zettl, and J. Clarke, Phys. Rev. B **49**, 16899 (1994).

[114] K. Nakanishi, J. Phys. Soc. Jpn. **43**, 1509 (1977).

[115] S. Urazhdin, D. Bilc, S. H. Tessmer, S. D. Mahanti, T. Kyratsi, and M. G. Kanatzidis, Phys. Rev. B **66**, 161306 (2002).

[116] Z. Rak, A. Tomic, S. D. Mahanti, and S. H. Tessmer, unpublished (2008).

[117] P. Hohenberg and W. Kohn, Phys. Rev. **136**, B864 (1965).

[118] D. J. Singh, *Plane Waves, Pseudopotentials and the LAPW Method*, Kluwer Academic Publishers, Boston, 1994.

[119] J. P. Perdew, K. Burke, and M. Ernzerhof, Phys. Rev. Lett. **77**, 3865 (1996).

[120] V. Brouet, unpublished (2007).

[121] D. M. Rowe, editor, *CRC Handbook of Thermoelectrics*, Chemical Rubber Press, Boca Raton, FL, 1995.

[122] M. G. Kanatzidis, S. D. Mahanti, and T. P. Hogan, *Chemistry, Physics, and Materials Science of Thermoelectric Materials: Beyond Bismuth Telluride*, Kluwer Academic/Plenum Publishers, 2002.

[123] T. M. Tritt and M. A. Subramanian, MRS Bulletin **31**, 188 (2006).

[124] A. F. Ioffe, Poluprovoduikovye Termoelementy, Moskow-Leningrad (1956).

[125] F. J. DiSalvo, Science **285**, 703 (1999).

[126] B. Wolfing, C. Kloc, J. Teubner, and E. Bucher, Phys. Rev. Lett. **86**, 4350 (2001).

[127] K. Kurosaki, A. Kosuga, H. Muta, M. Uno, and S. Yamanaka, Appl. Phys. Lett. **87**, 061919 (2005).

[128] M. G. Kanatzidis, Acc. Chem. Res. **38**, 359 (2005).

[129] K. Fujita, T. Mochida, and K. Nakamura, Jpn. J. Appl. Phys. **40**, 4644 (2001).

[130] S. Lambert, H. Leligny, and D. Grebille, J. Solid State Chem. **160**, 322 (2001).

[131] I. Terasaki, Y. Ishii, D. Tanaka, K. Takahata, and Y. Iguchi, Jpn. J. Appl. Phys. **40**, L65 (2001).

[132] G. S. Nolas, M. Kaeser, R. T. Littleton, and T. M. Tritt, Appl. Phys. Lett. **77**, 1855 (2000).

[133] Y. Miyazaki, X. Y. Huang, and T. Kajitani, J. Solid State Chem. **178**, 2973 (2005).

[134] J. Y. Son, B. G. Kim, and J. H. Cho, Appl. Phys. Lett. **86**, 221918 (2005).

[135] D. I. Bilc, S. D. Mahanti, T. Kyratsi, D.-Y. Chung, M. G. Kanatzidis, and P. Larson, Phys. Rev. B **71**, 085116 (2005).

[136] T. Kyratsi, E. Hatzikraniotis, K. M. Paraskevopoulos, C. D. Malliakas, J. S. Dyck, C. Uher, and M. G. Kanatzidis, J. Appl. Phys. **100**, 123704 (2006).

[137] M. G. Kanatzidis, Semicond. Semimet. **70**, 51 (2001).

[138] N. F. Mott and H. Jones, *Theory of the properties of metals and alloys*, Oxford University Press, London, 1936.

[139] P. L. Taylor, Phys. Rev. B **6**, 1197 (1973).

[140] K. Hoang and S. D. Mahanti, private communications (2007).